



## Article

# New Evidence of the Relationship Between Oxidative Hydrolysis of CuCl “Bronze Disease” and Relative Humidity (RH) for Management of Archaeological Copper Alloys

Johanna Thunberg <sup>\*</sup>, Nicola Emmerson  and David Watkinson

School of History, Archaeology and Religion, Cardiff University, Cardiff CF10 3EU, UK; emmersonnj@cardiff.ac.uk (N.E.); watkinson@cardiff.ac.uk (D.W.)

\* Correspondence: thunbergjc@cardiff.ac.uk

## Abstract

A key goal when managing copper alloy heritage is preventing “bronze disease,” which damages surface detail and may disintegrate objects by oxidation and hydrolysis of nanotokite (CuCl), forming voluminous copper trihydroxochlorides (Cu<sub>2</sub>(OH)<sub>3</sub>Cl). The success of mitigation strategies is difficult to evaluate due to the complexity of copper alloy corrosion profiles, limitations in non-destructive analytical methods and incomplete understanding of the corrosion mechanisms and reactions involved in bronze disease. Without better understanding, it is impossible to design truly effective solutions for the safe storage and display of archaeological copper alloys. Advancing current understanding, this paper examines oxidation and hydrolysis of CuCl using oxygen consumption, Fourier transform infrared spectroscopy and Raman spectroscopy, recognised as the basis of bronze disease. Variables potentially affecting bronze disease processes are evaluated, including relative humidity (RH) (15–80%RH at 20 °C) and the presence of metallic copper with CuCl and their respective ratios. Results confirm that these variables influence the reaction mechanisms and kinetics of bronze disease. The rate of oxidation and hydrolysis of CuCl accelerates with RH, and its effect is quantified. The presence of copper is shown to be important for producing bronze disease; it facilitates a cyclic reaction forming Cu<sub>2</sub>(OH)<sub>3</sub>Cl, increases its formation rate at lower RH than by hydrolysis of CuCl alone and prevents formation of soluble chloride compounds. The formation of Cu<sub>2</sub>(OH)<sub>3</sub>Cl without counteracting copper ions is shown to promote formation of CuCl<sub>2</sub> and CuCl<sub>2</sub>·2H<sub>2</sub>O, accelerating bronze disease. This new understanding is used to better quantify risk of bronze disease as a function of RH, providing a more quantitative tool for managing preservation of archaeological copper alloy collections.

**Keywords:** bronze disease; copper alloy; archaeological; relative humidity; management; risk; storage



Academic Editors: Giovanni E. Gigante and Nick Schiavon

Received: 9 May 2025

Revised: 22 August 2025

Accepted: 27 August 2025

Published: 28 August 2025

**Citation:** Thunberg, J.; Emmerson, N.; Watkinson, D. New Evidence of the Relationship Between Oxidative Hydrolysis of CuCl “Bronze Disease” and Relative Humidity (RH) for Management of Archaeological Copper Alloys. *Heritage* **2025**, *8*, 350. <https://doi.org/10.3390/heritage8090350>

**Copyright:** © 2025 by the authors. Licensee MDPI, Basel, Switzerland. This article is an open access article distributed under the terms and conditions of the Creative Commons Attribution (CC BY) license (<https://creativecommons.org/licenses/by/4.0/>).

## 1. Introduction

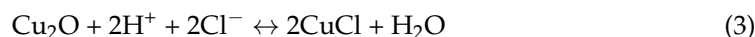
Long-term, sustainable and cost-effective management practices are essential for the preservation of archaeological copper and its alloys. Successful approaches must be underpinned by an understanding of the chemistry and structure of materials, of which environmental agencies of decay can trigger mechanisms of change, and of how to identify risk to individual objects and collections [1].

Corrosion fundamentally changes the nature of archaeological copper alloy objects, which are often excavated with complex corrosion profiles that either preserve or obscure

the intended shape of the object [1–3]. The burial environment plays a role in dictating the nature and properties of corrosion profiles and to what extent they are protective, reducing the likelihood of post-excavation deterioration, or a risk, supporting further corrosion [2–6]. If the burial environment contains free chlorides, it is possible that chloride complexes form within the corrosion stratigraphy. One of these complexes, copper (I) chloride (CuCl), has been linked to destructive changes in the post-excavation environment. CuCl is thought to form in low oxygen, slightly acidic soils by outward diffusion of  $\text{Cu}^+$  ions from the metallic copper and inward diffusion of chloride ions from the burial environment [7–9] ((1) and (2)):



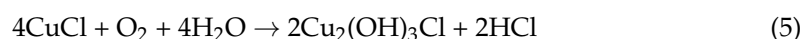
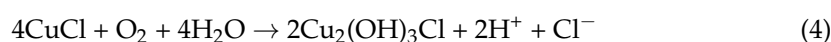
In favourable conditions, continuous dissolution of copper through formation of CuCl can cause complete mineralisation of objects [10]. In low pH environments (<5), CuCl can also form via basic copper (I) oxide ( $\text{Cu}_2\text{O}$ ) by interaction with hydrogen and chloride ions (3) [10–12].



The location of CuCl within corrosion profiles has important implications for the risk posed to objects in the post-excavation environment. It is mostly described and identified as adjacent to the metal core [13–17] in layers or as localised deposits [11,14,15,18–20]. CuCl has also been identified in isolation from the metal as “pockets” or “islands”, above a  $\text{Cu}_2\text{O}$  layer, in pits and in mineralised objects [16–18,21]. Hundreds, or thousands, of years in a burial environment where objects undergo slow changes towards thermodynamic equilibria mean that CuCl can remain a relatively stable compound, posing no significant risk to objects [16]. Many archaeological copper alloys are therefore excavated with CuCl remaining within the structure.

## 2. Post-Excavation Risk Mechanisms

Increased availability of oxygen and atmospheric water following excavation has been proven to enable recrystallisation of CuCl to copper trihydroxychloride polymorphs  $\text{Cu}_2(\text{OH})_3\text{Cl}$  [8,12,13,16,22]. Early efforts to examine their thermodynamics underpin a fundamental understanding of these reactions [18,23]. It is generally agreed that the recrystallisation of CuCl is of stoichiometry ((4) or (5)):



These processes are colloquially referred to as “bronze disease” [7,13,15,16,23] and present the predominant risk to archaeological copper alloys in the post-excavation environment. Despite its name, this loose transferable terminology is associated with  $\text{Cu}_2(\text{OH})_3\text{Cl}$  polymorphs and not the metallographic composition of the object on which it occurs.

The relative volumetric differences between CuCl and  $\text{Cu}_2(\text{OH})_3\text{Cl}$  during recrystallisation can cause stresses within the overlying corrosion structure, fragmenting otherwise coherent products as  $\text{Cu}_2(\text{OH})_3\text{Cl}$  erupts on the surface of objects (Figure 1). This causes loss of original material and can accelerate further corrosion by facilitating diffusion of soluble species through cracking or loss of secondary corrosion product layers.



**Figure 1.** Copper alloy coin displaying signs of bronze disease, illustrating the physical loss of original material and heritage value that can be caused by  $\text{Cu}_2(\text{OH})_3\text{Cl}$  formation.

Risk to objects may be aggravated by the ability of  $\text{CuCl}$  to form continuously if there is a source of metallic copper. The byproducts of formation of (4) and (5)  $\text{Cu}_2(\text{OH})_3\text{Cl}$ , i.e.,  $\text{H}^+$  and  $\text{Cl}^-$  ions, can react with copper to form  $\text{CuCl}$  ((6) and (7)):



This cyclic process will gradually deplete the metallic core and can cause extensive damage as  $\text{Cu}_2(\text{OH})_3\text{Cl}$  continues to form. Theoretically, these mechanisms will continue until all  $\text{CuCl}$  has recrystallised. This can have a catastrophic effect on objects if it progresses unnoticed.

Analysis of corrosion compounds and synthesis of  $\text{Cu}_2(\text{OH})_3\text{Cl}$  confirms that  $\text{Cu}_2(\text{OH})_3\text{Cl}$  has several polymorphs and that all can occur on archaeological copper alloy objects, forming according to their thermodynamical stability [24–27] (Table 1). This shows that  $\alpha\text{-Cu}_2(\text{OH})_3\text{Cl}$  (botallackite) forms first, followed by  $\beta\text{-Cu}_2(\text{OH})_3\text{Cl}$  (atacamite) and  $\gamma\text{-Cu}_2(\text{OH})_3\text{Cl}$  (clinoatacamite). Atacamite and clinoatacamite are often found together due to their similar stabilities [16]. Clinoatacamite is a relatively recently identified polymorph [28,29] and replaced paratacamite as the most thermodynamically stable phase in the  $\text{Cu}_2(\text{OH})_3\text{Cl}$  sequence, as paratacamite is now believed to require integration of Zn or Ni [28,30]. Examination of  $\text{Cu}_2(\text{OH})_3\text{Cl}$  formation through synthesis has shown that intrinsic variables such as  $\text{Cu}^{2+}$  and  $\text{Cl}^-$  ratios can influence which polymorph is formed [25–27,31].

**Table 1.** Polymorphs of  $\text{Cu}_2(\text{OH})_3\text{Cl}$  alongside calculated Gibbs free energy [25]. Note that clinoatacamite is referred to as paratacamite in citation as clinoatacamite was not a recognised polymorph at the time of publication [24,25].

Polymorph	Mineral Name	$\Delta G$ 298.2k (kJ mol <sup>−1</sup> )
$\alpha\text{-Cu}_2(\text{OH})_3\text{Cl}$	Botallackite	−1322.6
$\beta\text{-Cu}_2(\text{OH})_3\text{Cl}$	Atacamite	−1335.1
$\gamma\text{-Cu}_2(\text{OH})_3\text{Cl}$	Clinoatacamite	−1341.8

Questions remain about fundamental aspects of bronze disease and factors affecting its kinetics, which may further inform management procedures to prevent or control it. There is limited evidence of the role of copper in bronze disease. Anecdotally, there is

a misconception that bronze disease is only destructive in the presence of a metal core, yet metallic copper is not required for the formation of  $\text{Cu}_2(\text{OH})_3\text{Cl}$  where CuCl has formed within the corrosion profile of an object. The cyclical aspect of bronze disease facilitated by copper ions, whilst stoichiometrically possible, has only been tentatively proven experimentally [13]. Whether or not the presence of a metallic core has any other implication for bronze disease is not known.

Understanding of the full range of reactions that can occur, when and why they do so and their link to bronze disease is still developing. Whether recrystallisation of polymorphs has risk implications is unknown, and there are questions around the formation and impact of the rare higher complex chlorides, such as  $\text{CuCl}_2$  and  $\text{CuCl}_2 \cdot 2\text{H}_2\text{O}$  [32]. A relatively unknown compound,  $\text{Cu}(\text{OH})\text{Cl}$  (mineral name belloite), has been linked to the bronze disease process [26], but its role has not been examined. There is also an enigma around the occurrence of a green, acidic liquid related to bronze disease, perhaps similar to “weeping” in archaeological iron objects [15].

### 3. Management of Risk

The generally agreed-upon principles of bronze disease have enabled the development of practices to control and mitigate it. Removing CuCl by encouraging its transformation to stable or soluble compounds is possible [20,33–35], but success is difficult to quantify and monitor due to practical difficulties of locating CuCl within corrosion profiles [15], and consideration of the aesthetic impacts of treatments is required.

Barrier coatings or inhibitors may prevent the triggering mechanisms of oxygen and atmospheric water [36–40], but their application can require significant investment of time and alter the appearance of objects [41,42], pose health and safety concerns [43] and have implications for surface analysis. It is difficult to quantify long-term success of these treatments, and the compositions of commercial products are often unknown or can change without notice [35,39,44–47].

A common method for managing risk is restricting the interaction between objects and atmospheric moisture by desiccation, following the understanding that availability of water is critical for bronze disease (4), (5) [48–52]. In corrosion control, relative humidity (RH) is manipulated to do one of the following::

- Prevent corrosion from occurring altogether;
- Control the rate at which corrosion occurs.

This exploits the understanding that atmospheric water can support electrochemical corrosion by water adsorption, forming thin-layer electrolytes that permit ionic transport [53,54]. Water is also necessary for the transformation of CuCl to  $\text{Cu}_2(\text{OH})_3\text{Cl}$  polymorphs in bronze disease. A critical threshold RH at which sufficient water is adsorbed on a surface to support corrosion mechanisms is believed to exist. This value will vary depending on the reactivity and hygroscopicity of materials.

Identifying critical RH thresholds and understanding how corrosion kinetics are affected by RH is crucial for managing collections of archaeological metals. Whilst a relationship between RH and corrosion risk has been established for archaeological iron [48,55,56], evidence is inconsistent and conflicting for bronze disease. Attempts to identify a critical RH for bronze disease have produced a range of suggested values from 28%RH [22] to 63%RH [57]. The sector appears to adopt a midpoint, between 35–55%RH, for managing bronze disease [48,58]. Monitoring reaction rates across a comprehensive range of RH environments is necessary to establish how magnitude of risk changes with RH. This is particularly important for mixed materials storage and display contexts and where low RH cannot be achieved readily or monitored frequently [59].

Studies quantifying the effect of RH on bronze disease kinetics are limited and focus on reaction rates where CuCl is in contact with metallic copper [16,22], which does not fully represent the various locations of CuCl possible within corrosion profiles [16,22]. Examining other rate factors, such as relative amounts of CuCl and copper metal, has never been performed in atmospheric conditions.

The aim of this study is to further elucidate selected intrinsic and extrinsic factors affecting the mechanisms and kinetics of oxidative hydrolysis of CuCl, colloquially known as bronze disease. This has been achieved by the following:

- (1) Quantifying the response of CuCl and copper-CuCl powder mixtures between 15–80%RH using an oxygen consumption technique.
- (2) Characterising the products formed in (1) using Fourier transform infrared spectroscopy and Raman spectroscopy.

## 4. Method

### 4.1. Samples

Analytical grade powders were chosen to control variables that may affect hydrolysis and oxidation of copper (I) chloride (CuCl) and ensure standardisation and reproducibility. CuCl (Acros Organic 99% extra purified nitrogen flushed CuCl) was tested on its own and mixed with copper (Cu, Fisher Scientific 99% copper powder) in Cu-CuCl ratios of 1:1, 1:0.5 and 1:0.25 (Table 2). Masses of the reactants were chosen to produce detectable oxygen consumption and were weighed using a Sartorius Secura Semi-Micro Balance ( $0.01 \text{ mg} \pm 0.03 \text{ mg}$ ). To achieve similar particulate sizes and even distribution of Cu and CuCl in mixtures, all samples were ground in an agate pestle and mortar before being transferred to a diamond-shaped weigh boat ( $55 \text{ mm} \times 31 \text{ mm} \times 5 \text{ mm}$ ). Three identical setups were used in each test (Table 2). The oxygen consumption of three samples of copper powder (1 g) was measured at each RH as controls, as copper consumes oxygen to produce  $\text{Cu}_2\text{O}$ . The purity of CuCl was evaluated with FTIR and Raman spectroscopy using the protocol provided below.

**Table 2.** Sample ratios and time subjected to oxygen consumption at a given RH value. Temperature is fixed at  $20^\circ\text{C}$  in all tests. All samples prepared in triplicate.

RH%	Sample ( $\text{x}^3$ )	Ratio Cu:CuCl (g)	Measurement Time (days)
15	1 g Cu 0 g CuCl	1:0	97
	1 g Cu 1 g CuCl	1:1	153
	0 g Cu 0.25 g CuCl	0:25	118
	1 g Cu: 0.25 g CuCl	1:0.25	200
20	1 g Cu 0.5 g CuCl	1:0.5	137
	1 g Cu 1 g CuCl	1:1	138
	1 g Cu 0 g CuCl	1:0	97
	0 g Cu 0.25 g CuCl	0:25	395
30	1 g Cu 0.25 g CuCl	1:0.25	126
	1 g Cu 0.5 g CuCl	1:0.5	130
	1 g Cu 1 g CuCl	1:1	130
	1 g Cu 0 g CuCl	1:0	37
40	0 g Cu 0.25 g CuCl	0:25	537
	1 g Cu 0.25 g CuCl	1:0.25	75
	1 g Cu 0.5 g CuCl	1:0.5	74
	1 g Cu 1 g CuCl	1:1	53
	1 g Cu 0 g CuCl	1:0	37

Table 2. *Cont.*

RH%	Sample (x <sup>3</sup> )	Ratio Cu:CuCl (g)	Measurement Time (days)
50	0 g Cu 0.25 g CuCl	0:25	551
	1 g Cu 0.25 g CuCl	1:0.25	65
	1 g Cu 0.5 g CuCl	1:0.5	48
	1 g Cu 1 g CuCl	1:1	27
	1 g Cu 0 g CuCl	1:0	15
60	0 g Cu 0.25 g CuCl	0:25	143
	1 g Cu 0.25 g CuCl	1:0.25	17
	1 g Cu 0.5 g CuCl	1:0.5	13
	1 g Cu 1 g CuCl	1:1	14
	1 g Cu 0 g CuCl	1:0	13
65	0 g Cu 0.25 g CuCl	0:0.25	21
	1 g Cu 0.25 g CuCl	1:0.25	17
	0 g Cu 0.25 g CuCl	0:25	5
70	1 g Cu 0.25 g CuCl	1:0.25	5
	1 g Cu 0.5 g CuCl	1:0.5	4
	1 g Cu 1 g CuCl	1:1	2
	1 g Cu 0 g CuCl	1:0	5
	0 g Cu 0.25 g CuCl	0:25	2
80	1 g Cu 0.25 g CuCl	1:0.25	3
	1 g Cu 0.5 g CuCl	1:0.5	2
	1 g Cu 1 g CuCl	1:1	1
	1 g Cu 0 g CuCl	1:0	3

#### 4.2. Environments

Samples were exposed to RH between 15–80%RH at 20 °C to investigate how the amount of atmospheric water affects the rate of oxidation and hydrolysis of CuCl. The RH range was chosen to represent typical collection storage and display environments. Increments of 10%RH were generally examined except for the lowest RH (15%RH), which was determined to be the lowest RH that could be achieved reliably within the experimental protocol (below), and another test was conducted at 65%RH to gain more detail about the significant acceleration of corrosion rates around this RH. Temperature was static at 20 °C in all tests to isolate the effect of RH. A separate study has examined how temperature affects the rate of bronze disease mechanisms [60].

#### 4.3. Oxygen Consumption

For reactions involving oxygen, recording its consumption can provide a measure of corrosion. The technique used in this study monitors oxygen consumption by recording oxygen levels within an enclosed space through dynamic quenching of the fluorescence of a sensor spot. It uses a luminescent source that incites fluorescence by exciting luminophores in an oxygen sensitive complex. Oxygen molecules quench the fluorescence, generating a quantifiable measure of oxygen that is proportional to the emitted fluorescence.

Each test was set up in a 250 mL Mason Ball jar to create an airtight environment for oxygen measurements. The leakage rate of these has been proven to be low ( $\pm 0.0038$  mg O<sub>2</sub>/day) [61,62]. A two-point calibrated PreSens GmbH (Regensburg, Germany) SP-PSt3-NAU-D5-YOP ruthenium oxygen sensor spot was adhered to the interior wall of each vessel using Radio Spares (London, UK) RTV silicone rubber compound. A PreSens GmbH (Regensburg, Germany) POF-L2.5-1SMA 505 nm fibre sensor connected to a Fibox 4 (PreSens GmbH, Regensburg, Germany) oxygen meter was used as the luminescence source. At normal atmospheric oxygen pressure (207 hPa), the resolution of the oxygen spot is  $\pm 1$  hPa. This error decreases at lower oxygen levels to  $\pm 0.01$  hPa at 2 hPa.



The accuracy varies between  $\pm 4$  hPa at normal atmospheric oxygen pressure and  $\pm 0.5$  hPa at 2 hPa.

Each oxygen consumption vessel was filled with conditioned silica gel to maintain the desired RH throughout the test period and to reduce the headspace in the jar, increasing the potential for measurable oxygen consumption [62]. Silica gel was conditioned to a constant weight in a Binder (Tuttlingen, Germany) KBF720 climate chamber at each test RH and 20 °C ( $\pm 1.5\%$  RH and  $\pm 0.1$  °C). Two-point calibrated MadgeTech 101 A dataloggers ( $\pm 1.9\%$  RH and  $\pm 0.2$  °C) were placed in the silica gel for a minimum of 24 h to confirm that the desired RH had been achieved.

The mass of silica gel within each vessel was determined at each RH to ensure that the volume of silica gel remained consistent in all setups (Table 3). A MadgeTech 101 A datalogger was placed in the silica gel, and the weigh boat containing the sample was placed on top of the silica gel (Figure 2) before the vessels were closed.

**Table 3.** Mass of silica gel included in oxygen consumption vessels at 20 °C at different RH.

RH	% Increase	Mass (g)
15	0	127.0
20	2.36	130.0
30	6.85	135.7
40	12.2	142.5
50	17.89	149.7
60	22.59	155.7
70	24.57	158.2
80	25.35	159.2
90	26.06	160.1



**Figure 2.** Vessel setup showing the placement of oxygen sensor spot, silica gel, datalogger and sample within oxygen consumption vessel.

Each vessel was positioned so that the tip of the fibre optic probe attached to the meter was aligned to the oxygen sensor spot within the vessel. Vessels and meters were placed in a Binder KBF720 where RH and temperature remained constant (50% RH, 20 °C,  $\pm 1.5\%$  RH and  $\pm 0.1$  °C) [62].

The accuracy of oxygen consumption as a measure of corrosion is affected after about 17 mg of oxygen has been consumed as an effect of the drop in oxygen pressure [22]. When this threshold was approached, either tests were terminated or vessels were reoxygenated. Reoxygenation was undertaken by opening the vessel, emptying and replacing the con-

tents and reclosing the vessel before resuming logging. Where corrosion rates were slow, measurements were continued for as long as feasible (Table 2).

#### 4.4. Data Processing

To account for volumetric differences between samples, all data has been calculated to oxygen consumed in milligrams using the ideal gas law (8):

$$PV = nRT \quad (8)$$

where  $P$  is pressure in atmospheres,  $V$  is volume in litres,  $n$  is amount of substance in mol,  $R$  is the ideal gas constant and  $T$  is temperature in Kelvin.

#### 4.5. Determining Rate

Examination of corrosion rates compared the dynamic oxygen consumption over time and generated an oxygen consumption rate (OCR) coefficient (determined as oxygen consumed in  $\text{mg}/\text{day}^{-1}$ ). Generating a single value provides a comparable measure that illustrates differences in corrosion rates caused by the examined variables, but to identify a corrosion rate coefficient, the assumption must be that corrosion rates are linear. The average oxygen consumption rate has therefore been calculated where all samples show a degree of linearity, neglecting other phases where rates may vary. The corrosion rate coefficient was always calculated from the final phase of corrosion rates before tests were terminated or no more oxygen consumption took place (Figure 3). The final oxygen consumption rate values are the mean of three samples.

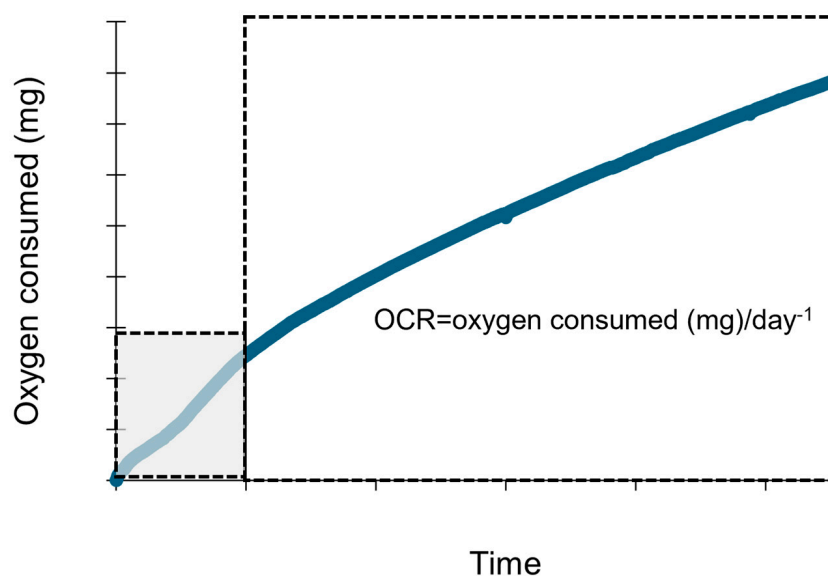


**Figure 3.** Example of typical oxygen consumption pattern illustrating where oxygen consumption coefficient was determined, ignoring variation in rate preceding this phase (marked in grey).

#### 4.6. Characterisation

Samples were qualitatively characterised at the end of each test by Fourier transform infrared spectroscopy (FTIR) and Raman spectroscopy. Three samples from each powder mixture were analysed by collecting powder ( $1 \text{ mg} \pm 0.2 \text{ mg}$ ) from the surface of each weighing boat with a 3 mm round synthetic brush. Samples were immediately placed in desiccated silica gel ( $1\% \pm 1.9 \text{ RH}$ ) after sampling and before analysis.



#### 4.6.1. Fourier Transform Infrared Spectroscopy

A Perkin Elmer Frontier Fourier Transform Infrared Spectrometer equipped with a diamond Attenuated Total Reflection (ATR) accessory was used for characterisation of all samples, analysing over the wavenumber range 4000–380  $\text{cm}^{-1}$ . Before analysis, the crystal was cleaned with Industrial Methylated Spirits (IMS) and the background collected in the Spectrum 10 software. Twenty scans were collected for each sample. Between each analysis, the crystal was cleaned with IMS. No spectral processing was conducted.

#### 4.6.2. Raman Spectroscopy

A B&W Tek iRaman equipped with a green 532 nm 30 mW laser was applied to selected samples for additional characterisation. Samples were analysed through an infinity-corrected long working distance planachromatic lens using a 20 $\times$  objective yielding a 105  $\mu\text{m}$  spot size. Laser output was between 0.3 mW and 0.9 mW, and analysis time was between 60 and 180 s. No spectral processing was conducted.

### 5. Results

#### 5.1. Oxygen Consumption

In all samples, oxygen consumption rates (OCR) are not linear but vary across several phases. The number of phases, their duration and typical rates vary with the presence of copper, the amount of CuCl in samples and the RH of the environment. As a rule of thumb, the duration and number of the different phases decreases with increasing RH and increasing proportion of CuCl in Cu:CuCl mixtures. Samples comprising CuCl mixed with copper have a greater number of phases (Figure 4).

Examining overall trends and calculating the OCR ( $\text{mg}/\text{day}^{-1}$ ) in all samples shows that the rate of oxygen consumption in samples depends on the following:

- The relative humidity;
- The presence or absence of metallic copper;
- The ratio of CuCl.

#### 5.2. Relative Humidity

Relative humidity thresholds for oxygen consumption are different depending on the samples. CuCl samples demonstrate measurable oxygen consumption between 30%RH and 80%RH. Oxygen consumption is recorded in all ratios of Cu:CuCl between 15%RH and 80%RH (Figures 4 and 5).

An exponential increase in OCR from the lowest RH at which oxygen consumption is recorded is evident in all samples ( $R^2 = 0.9626$ ), with Cu:CuCl in a 1:1 ratio showing the best fit to an exponential model ( $R^2 = 0.9982$ ) and CuCl without copper samples demonstrating the poorest fit ( $R^2 = 0.8902$ ) (Figures 4–6).

Increasing the RH in 10% increments results in acceleration of OCR up to 3.5 $\times$  (Figure 7A). The exception to this is a steep increase in OCR between 60 and 70%RH, which represents the most significant acceleration of OCR across the examined RH range, with an increase in OCR between 4 (Cu:CuCl 1:0.25) and 172 (CuCl) times (Figure 7A). The cumulative rise in OCR with RH from the lowest RH at which oxygen consumption is measured further illustrates the exponential rise in OCR with increasing RH and demonstrates the large magnitude of change in OCR with RH. From 20%RH to 80%RH, the OCR increases by more than 300 times in Cu:CuCl samples. Between 30%RH and 80%RH, the same value increases by 10,000 in CuCl samples (Figure 7B).

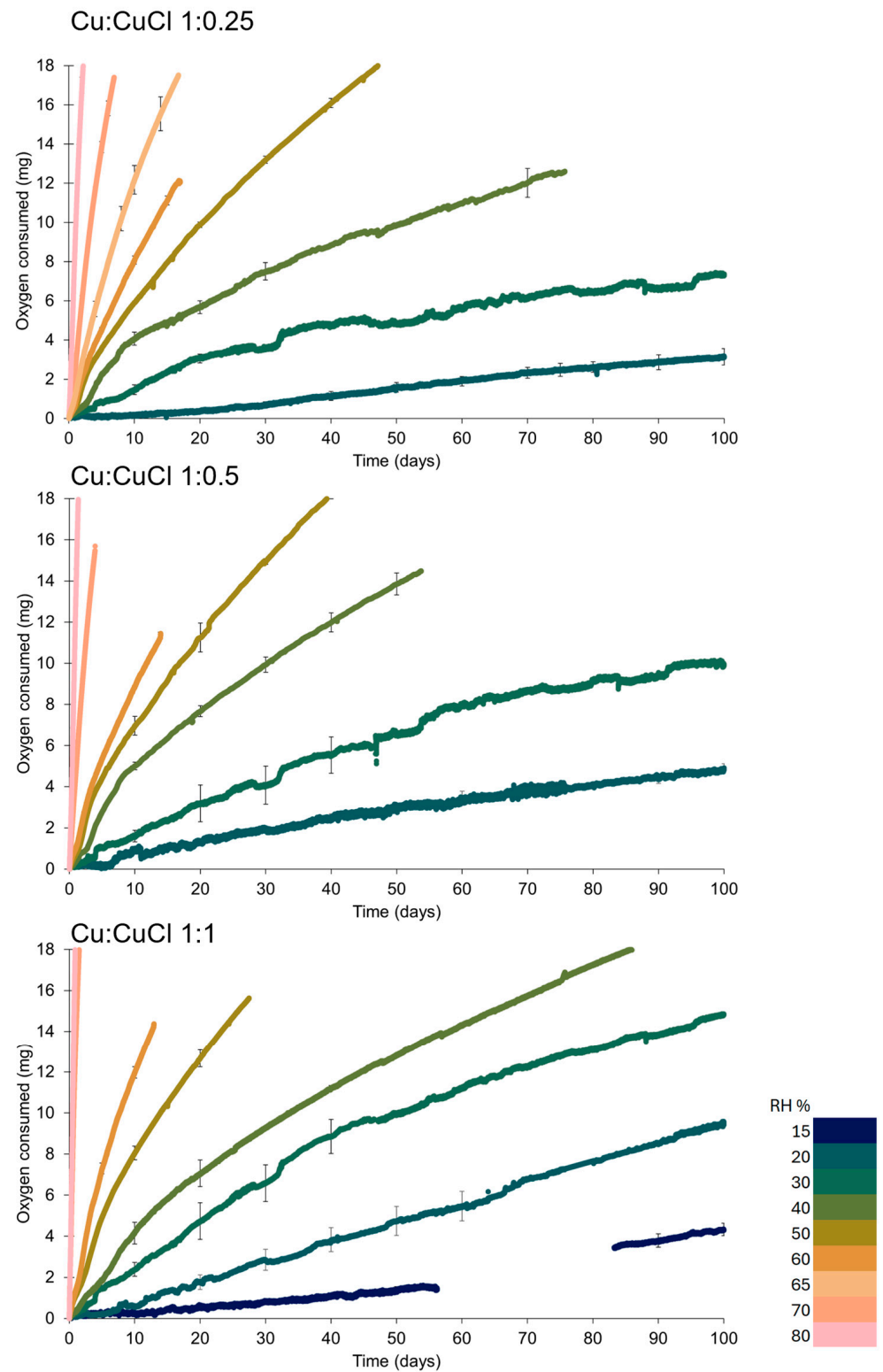


**Figure 4.** Oxygen consumption of different Cu:CuCl ratios across the examined range of RH at 20 °C. Each line is the average of three samples with error bars representing the SD at regular intervals.

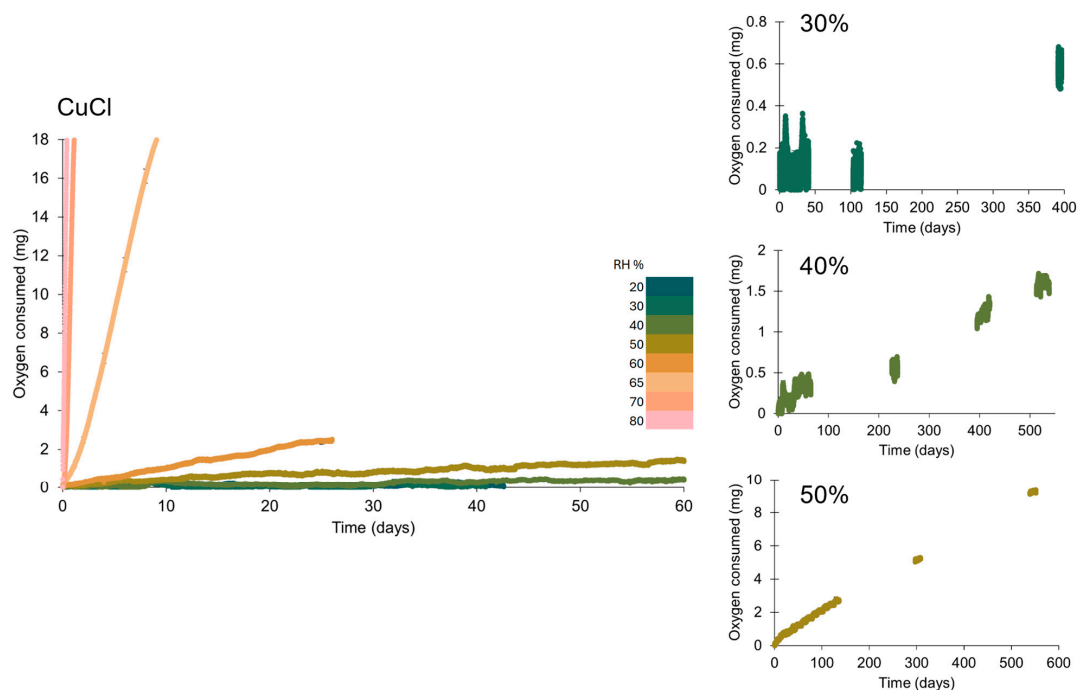


**Figure 5.** Oxygen consumption of CuCl across 20–80%RH at 20 °C. Inserts illustrate long-term oxygen consumption of samples between 30 and 50%RH. Each line is the average of three samples with error bars representing the SD at regular intervals.

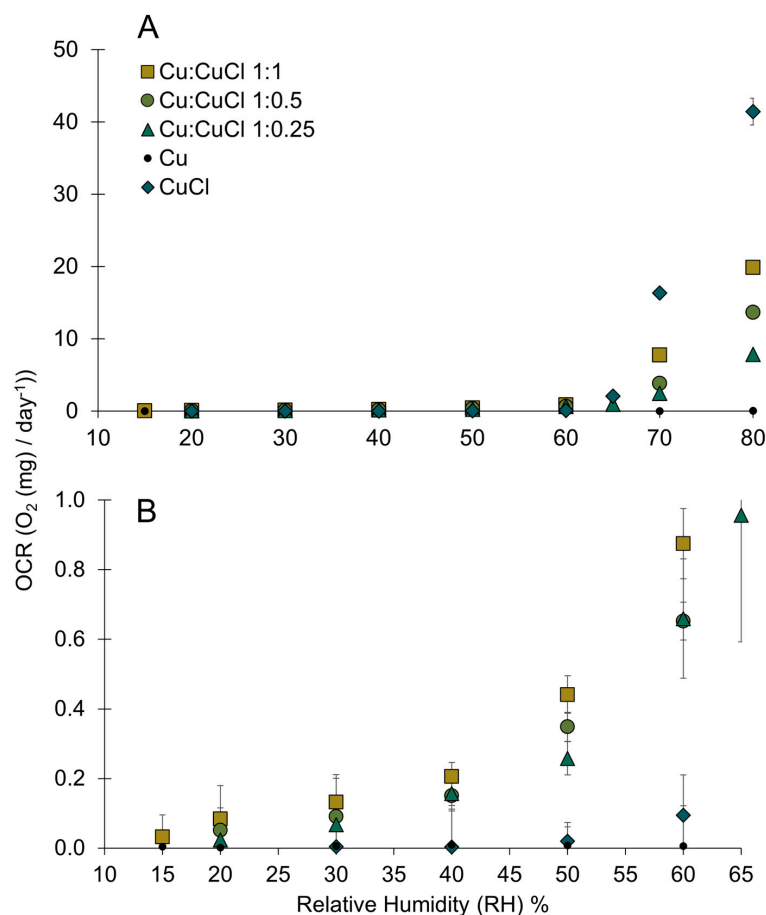


**Figure 6.** (A) OCR values calculated as the oxygen is consumed in mg per day. (B) Detail of OCR between 15%RH and 65%RH. Error bars are given as SD.

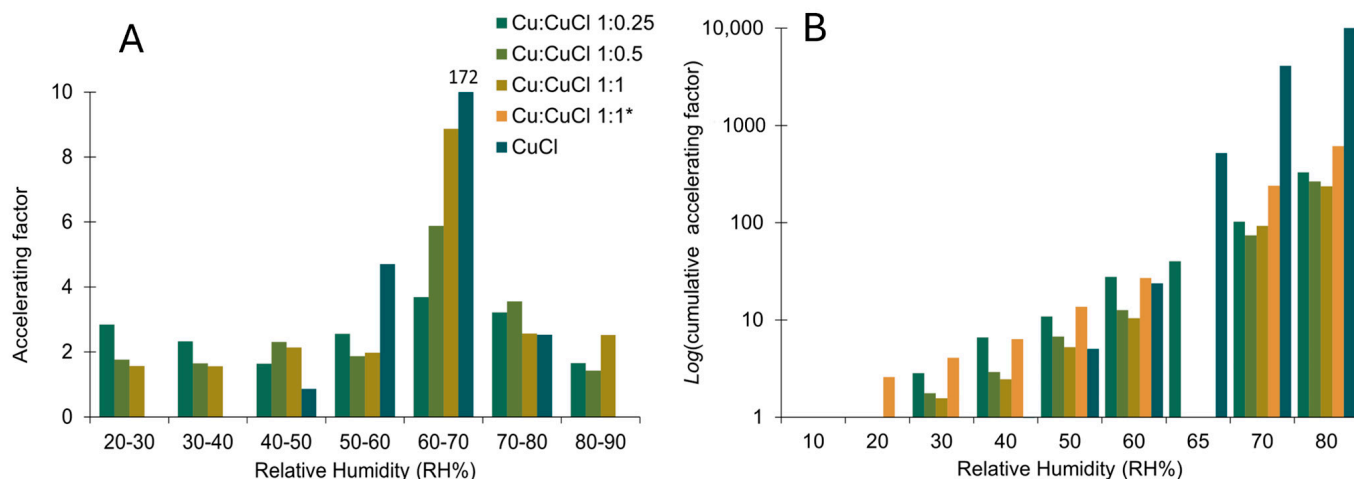


**Figure 7.** The effect of changing RH on OCR. (A) Mean accelerating factor when RH is raised in 10%RH increments. (B) Mean cumulative acceleration in OCR. Note that the accelerating factors are plotted in  $\text{Log}_{10}$  for ease of visualisation. The Cu:CuCl 1:1 is calculated twice, from 15%RH and 20%RH, to compare the effect of the ratio Cu:CuCl when RH is manipulated. \* denotes Cu:CuCl 1:1 calculated from 15%RH.

The effect of increasing the RH in 10% intervals becomes more significant for CuCl than for CuCl mixed with copper above 50%RH. The most significant difference occurs when the RH increases from 60%RH to 70%RH, when the OCR of CuCl increases 172 times (Figure 7A). When the same quantity of CuCl is mixed with copper (Cu:CuCl 1:0.25), the OCR increases four times between 60–70%RH. This is also apparent in the cumulative accelerating effect from the lowest RH at which oxygen is consumed (Figure 7B).

The rate of oxygen consumption is greater where CuCl is mixed with copper up to 60%RH. The greatest difference is seen at 40%RH where the OCR of CuCl in contact with copper is 45 times faster than with the same quantity of CuCl without copper (Figure 8). At 65%RH and above, CuCl demonstrates a more rapid OCR without the presence of copper, up to seven times faster at 70%RH (Figure 8).

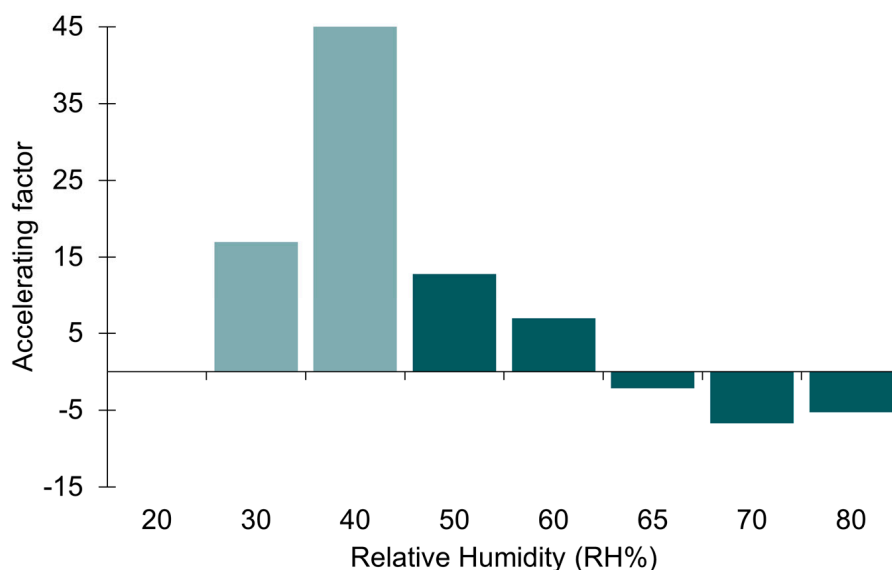


**Figure 8.** Illustrating the accelerating effect of copper on OCR when CuCl is in proximity to copper metal. The lighter colour denotes the lack of evidence to support  $\text{Cu}_2(\text{OH})_3\text{Cl} \leq 40\% \text{RH}$  without the presence of copper (see characterisation below).

Comparing the OCR of Cu:CuCl in different ratios, it is evident that increasing the amount of CuCl results in an overall faster OCR rate at any given RH (Figure 9). In general, doubling the amount of CuCl doubles the OCR. Doubling the amount of CuCl again can accelerate OCR by up to 3.5 times at a given RH, but the total impact is RH dependent (Figure 10).

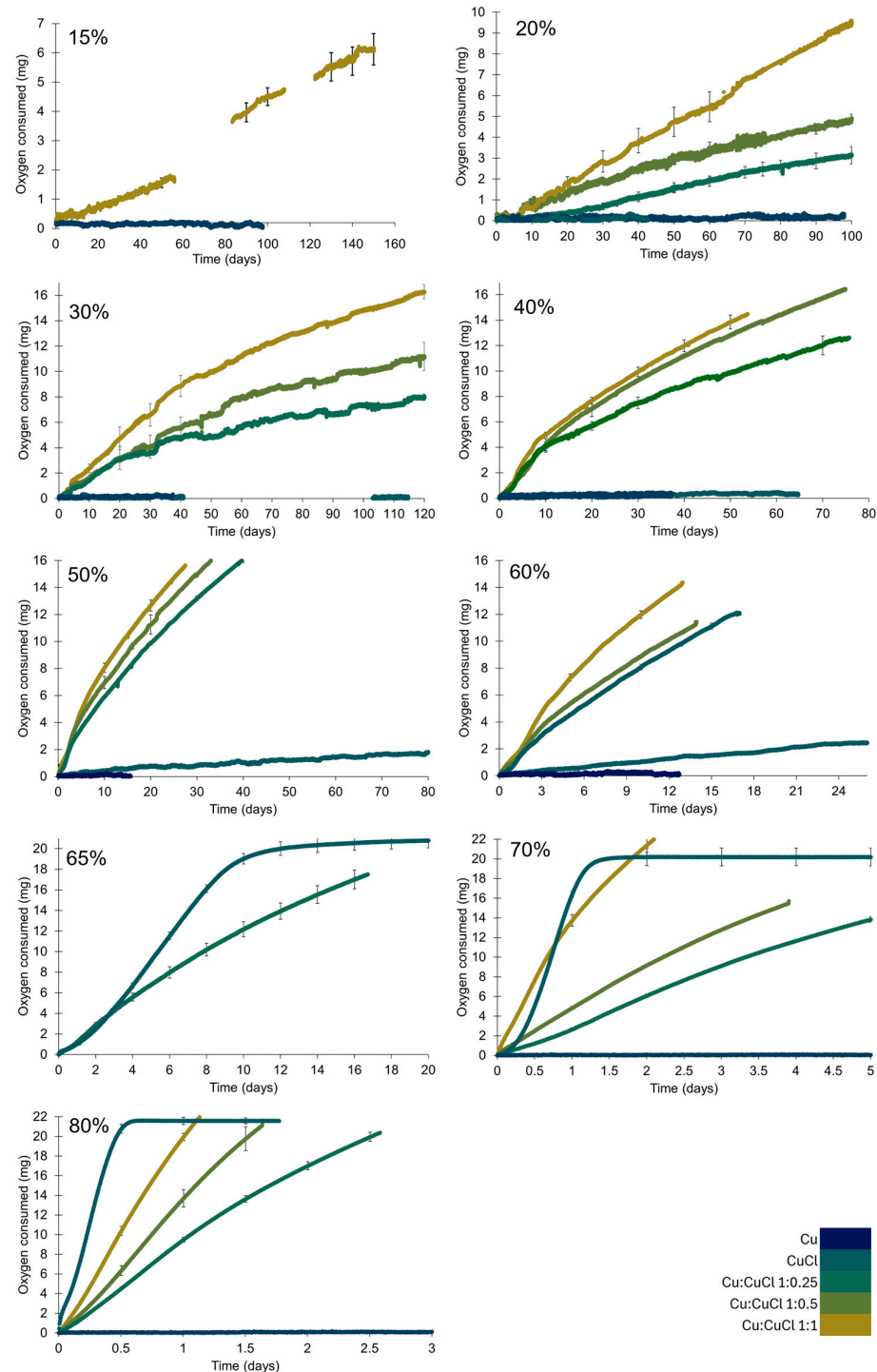


**Figure 9.** Oxygen consumption rates of all samples at different RHs, illustrating differences in OCR between CuCl and Cu:CuCl mixtures of different ratios. Copper controls are included. Error bars represent SD of three samples at regular time intervals.

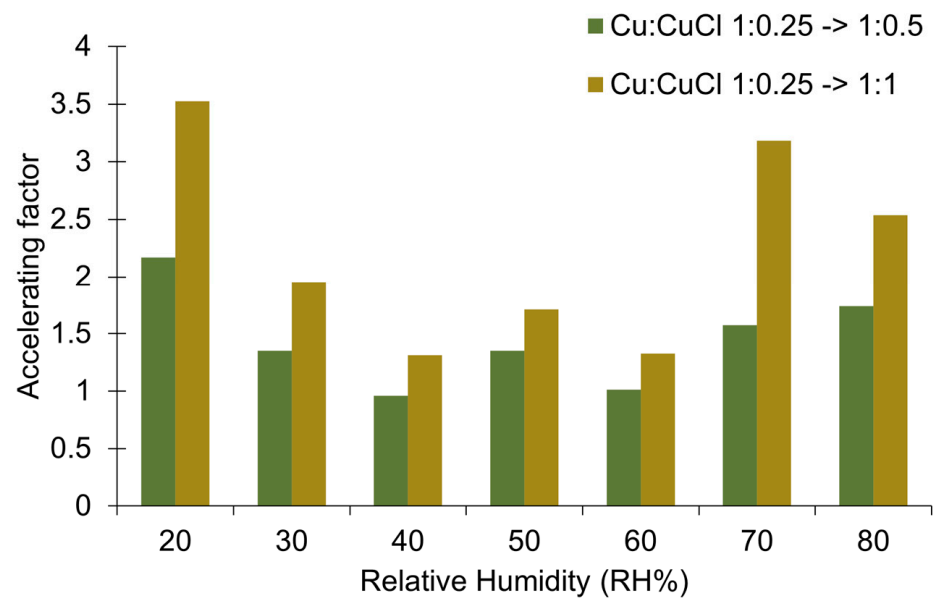


**Figure 10.** The accelerating effect of doubling the amount of CuCl and increasing the ratio Cu:CuCl at different RH.

The presence of copper affects the point at which oxygen consumption ceases. When vessels are regularly reoxygenated, an endpoint for CuCl samples occurs when 20–22 mg of oxygen have been consumed. When copper is mixed with CuCl, samples that have been regularly reoxygenated consume oxygen beyond this value. Comparing the oxygen consumption at 70%RH demonstrates this effect (Figure 11). The OCR in Cu:CuCl samples begins to reduce after ~30 mg of oxygen has been consumed.

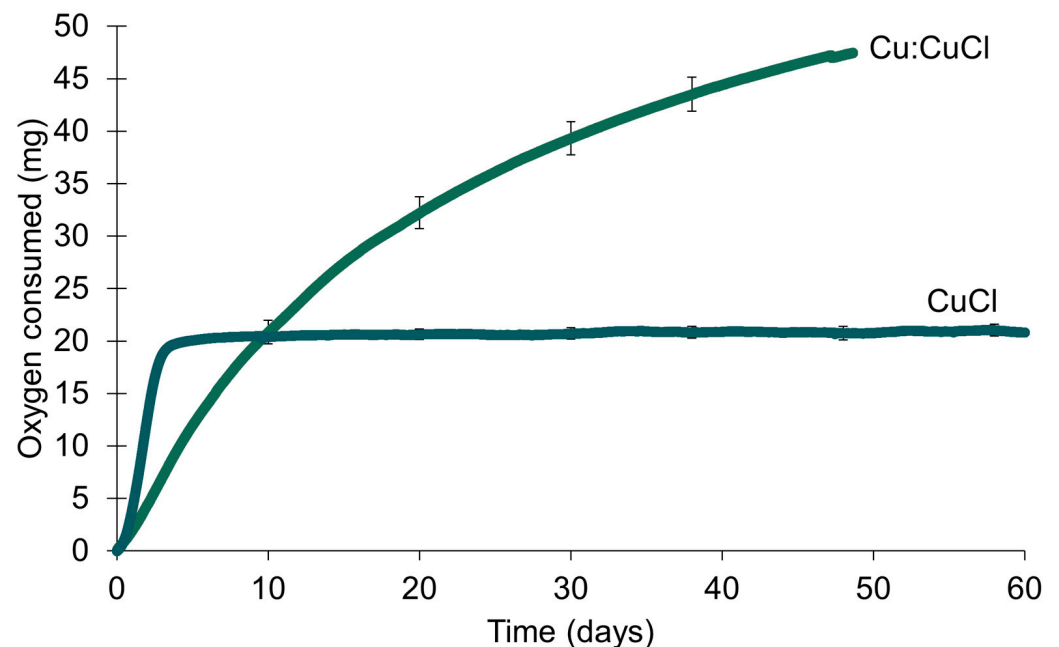


**Figure 11.** OCR of CuCl and Cu-CuCl samples at 70%RH where vessels are reoxygenated on days 9, 26 and 42, illustrating CuCl endpoint (blue) and the effect of copper in close proximity to CuCl (Cu:CuCl, green) on continuing the oxygen consumption process. Error bars represent the SD of three samples at regular intervals.



### 5.3. Sample Characterisation

Sample characterisation demonstrated that the CuCl powder contained an unknown quantity of Cu(OH)Cl before use. Different Cu<sub>2</sub>(OH)<sub>3</sub>Cl polymorphs and higher copper chloride species were additionally identified in samples that consumed oxygen. The products formed varied with the composition of samples and the RH at 20 °C (Table 4). A detailed description of the results is provided below.

**Table 4.** Summary of compounds identified by FTIR and Raman spectroscopy, with major compounds listed first where a mixture is identified. \* indicates where analysis suggests that a structural change to the compound has occurred.

RH%	CuCl	Cu:CuCl
0		CuCl, Cu(OH)Cl
15		Cu(OH)Cl *
20	CuCl, Cu(OH)Cl	γ-Cu <sub>2</sub> (OH) <sub>3</sub> Cl, β-Cu <sub>2</sub> (OH) <sub>3</sub> Cl
30	Cu(OH)Cl *	γ-Cu <sub>2</sub> (OH) <sub>3</sub> Cl, β-Cu <sub>2</sub> (OH) <sub>3</sub> Cl
40	Cu(OH)Cl *	γ-Cu <sub>2</sub> (OH) <sub>3</sub> Cl, β-Cu <sub>2</sub> (OH) <sub>3</sub> Cl
50	Cu(OH)Cl *, β,γ-Cu <sub>2</sub> (OH) <sub>3</sub> Cl, CuCl <sub>2</sub>	γ-Cu <sub>2</sub> (OH) <sub>3</sub> Cl, β-Cu <sub>2</sub> (OH) <sub>3</sub> Cl
60	Cu(OH)Cl *, β,γ-Cu <sub>2</sub> (OH) <sub>3</sub> Cl, CuCl <sub>2</sub>	γ-Cu <sub>2</sub> (OH) <sub>3</sub> Cl, β-Cu <sub>2</sub> (OH) <sub>3</sub> Cl
65	Cu(OH)Cl	γ-Cu <sub>2</sub> (OH) <sub>3</sub> Cl, β-Cu <sub>2</sub> (OH) <sub>3</sub> Cl
70	CuCl <sub>2</sub> , CuCl <sub>2</sub> ·2H <sub>2</sub> O, β-Cu <sub>2</sub> (OH) <sub>3</sub> Cl	γ-Cu <sub>2</sub> (OH) <sub>3</sub> Cl
80	CuCl <sub>2</sub> , CuCl <sub>2</sub> ·2H <sub>2</sub> O, β-Cu <sub>2</sub> (OH) <sub>3</sub> Cl	γ-Cu <sub>2</sub> (OH) <sub>3</sub> Cl

### 5.4. Unexposed CuCl

Peaks in the Raman spectra of unexposed samples of CuCl at 115 cm<sup>−1</sup> and 150 cm<sup>−1</sup> are tentatively assigned to Cu-Cl lattice vibrations. The peak at 462 cm<sup>−1</sup> may be associated with Cu-Cl in CuCl [63], but the combined peaks of O-H stretching at 3376 cm<sup>−1</sup> and diagnostic lattice modes at 462 cm<sup>−1</sup> and 386 cm<sup>−1</sup> and 310 cm<sup>−1</sup> can also indicate the presence of Cu(OH)Cl (mineral name belloite) [64] (Figure 12A). FTIR confirmed the presence of Cu(OH)Cl with characteristic peaks visible as O-H stretchings at 3456 cm<sup>−1</sup>, 3384 cm<sup>−1</sup> and 3220 cm<sup>−1</sup> and O-H bending at 903 cm<sup>−1</sup>, 851 cm<sup>−1</sup> and 805 cm<sup>−1</sup>. Peaks at 442 cm<sup>−1</sup>, 406 cm<sup>−1</sup> and 398 cm<sup>−1</sup> are associated with the Cu lattice modes of Cu(OH)Cl, including Cu-O, Cu-O-H, Cu-O-Cu and Cu-Cl-Cu but have not been assigned (Figure 12B) [65–68]. An O-H-O peak around 1610 cm<sup>−1</sup> and a weak O-H peak at 1240 cm<sup>−1</sup> could indicate some water adsorption but have also been associated with Cu-Cl [69].

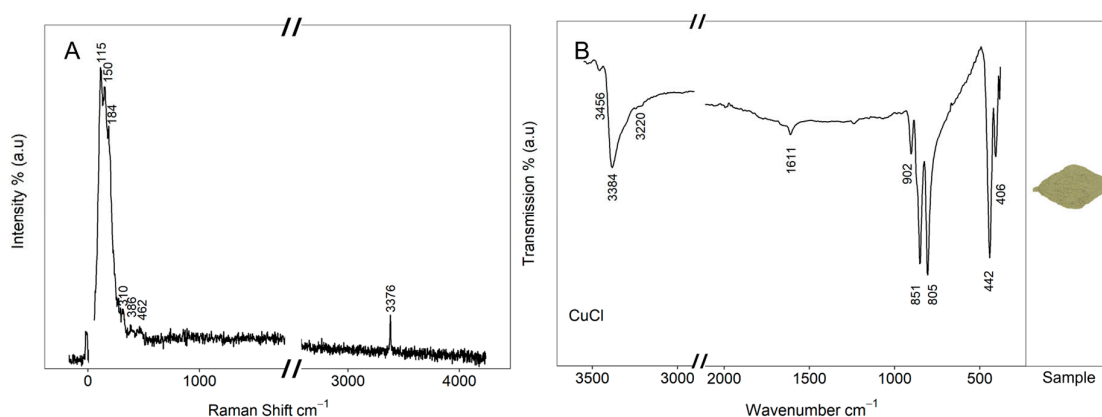


**Figure 12.** (A) Raman and (B) FTIR spectra of unexposed CuCl samples stored in a desiccated environment.

### 5.5. CuCl

There is no evidence of  $\text{Cu}_2(\text{OH})_3\text{Cl}$  in CuCl samples  $\leq 50\%\text{RH}$  (Figures 13 and 14 (A–D)). At 20%RH, no structural change is evident after 118 days (Figure 13). At 30%RH and 40%RH, some alteration of CuCl is evident with peak shifts and the appearance of new peaks (Figure 14 (A–D)). Peak shifts to lower wavenumbers are evident in the O–H stretching region over  $3000\text{ cm}^{-1}$ , and new O–H bending modes can be seen at  $988\text{ cm}^{-1}$ . Cu–O–H and O–Cu–O symmetric stretches are evident at  $586\text{ cm}^{-1}$  and  $513\text{ cm}^{-1}$ . The relative peak intensity of these bends and stretches increases towards the edges of the samples (Figure 14 (B,D)).

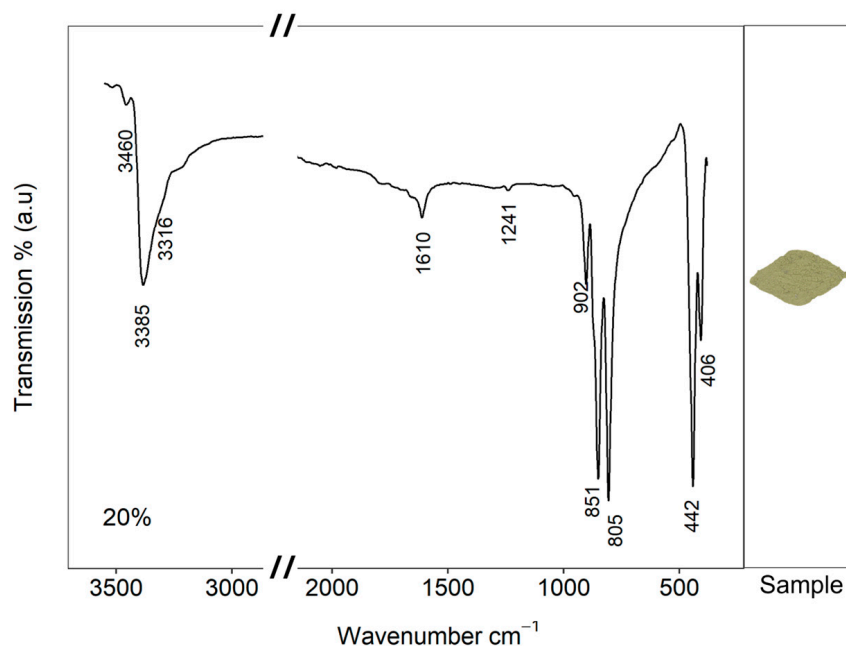


**Figure 13.** Representative CuCl sample 20%RH and 20 °C after 118 days, showing presence of  $\text{Cu}(\text{OH})\text{Cl}$ . Refer to Table 2 for experimental timeframes.

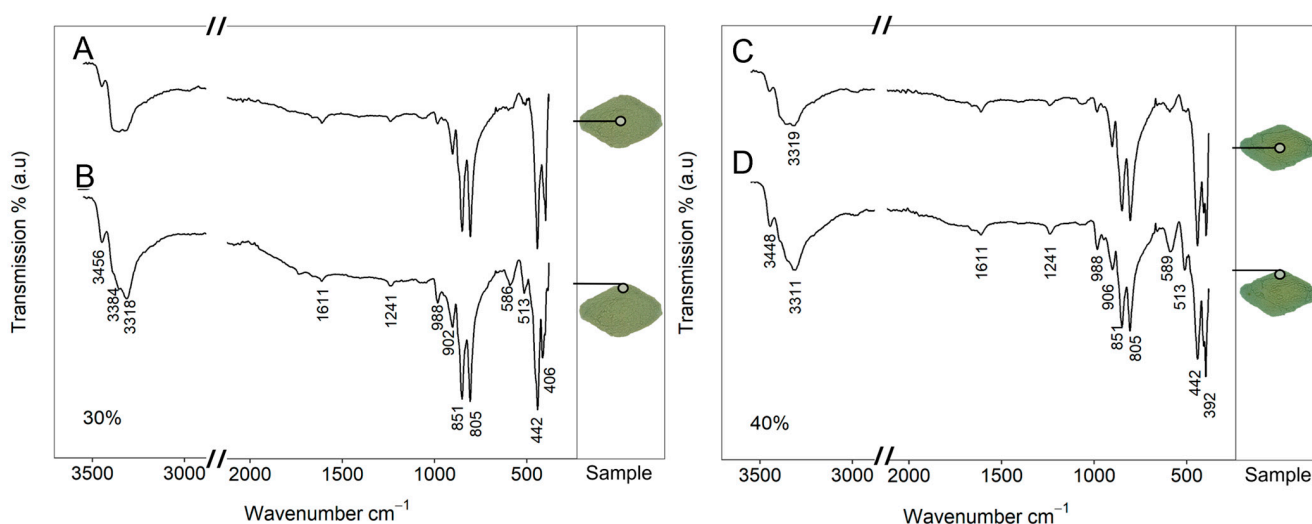


**Figure 14.** Representative CuCl samples between 30–40%RH and 20 °C with diagnostic peaks labelled. Samples show altered  $\text{CuCl}/\text{Cu}(\text{OH})\text{Cl}$  compound after exposure to 30%RH (A,B) and 40%RH (C,D). Peak locations in (A,B) and (C,D) are the same and have therefore only been labelled once. Refer to Table 2 for experimental timeframes.

At 50%RH and 60%RH, the bulk of samples suggest that a similar alteration of CuCl has taken place, but peak shifts and new peaks are evident towards the edges of samples (Figure 15 (A–D)), which indicate formation of  $\beta$ - and  $\gamma$ - $\text{Cu}_2(\text{OH})_3\text{Cl}$  polymorphs. O-H stretches above  $3000\text{ cm}^{-1}$  have shifted to lower wavenumbers with a shoulder appearing around  $3365\text{ cm}^{-1}$ . This is accompanied by an O-H bending mode at  $988\text{ cm}^{-1}$  and the appearance of Cu-O-H stretches around  $943\text{ cm}^{-1}$ ,  $920\text{ cm}^{-1}$  and  $828\text{ cm}^{-1}$ . Cu-O-H and O-Cu-O stretches around  $585\text{ cm}^{-1}$  and  $510\text{ cm}^{-1}$  also appear relatively stronger towards the edge of samples after exposure to these RH values (Figure 15 (B,D)) [26,70]. A peak at  $1583\text{ cm}^{-1}$  is evident (Figure 15 (A,C)) that may represent the formation of  $\text{CuCl}_2$ .

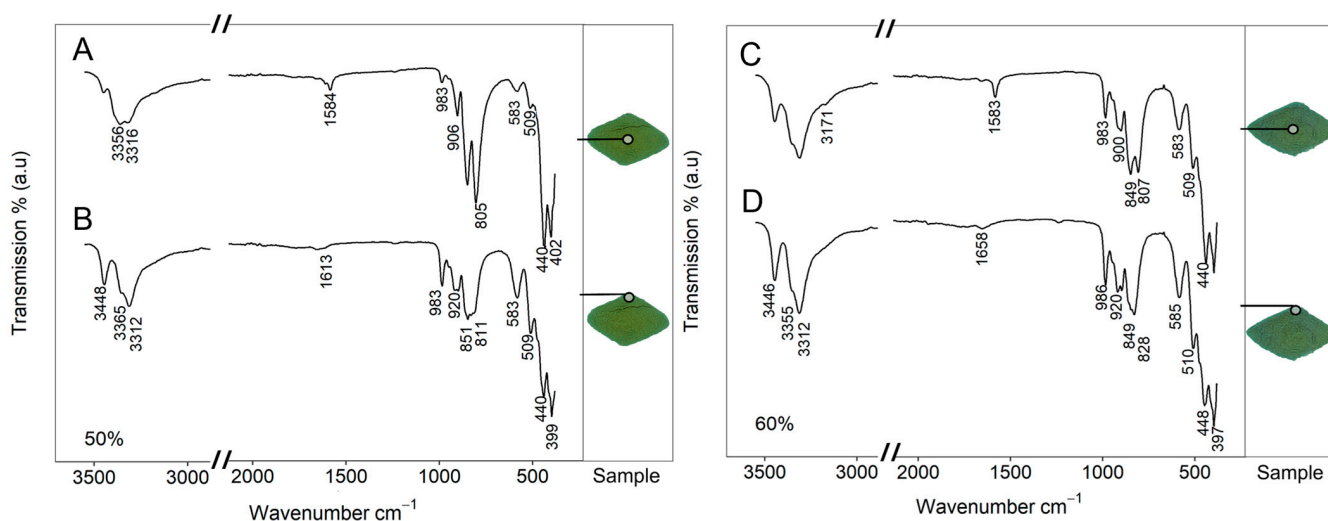


**Figure 15.** Representative CuCl samples at 50–60%RH and  $20\text{ }^{\circ}\text{C}$  with diagnostic peaks labelled. Samples show altered CuCl/Cu(OH)Cl and possible formation of  $\beta$ - and  $\gamma$ - $\text{Cu}_2(\text{OH})_3\text{Cl}$  towards the edge of the samples after exposure to 50%RH (A,B) and 60%RH (C,D). Refer to Table 2 for experimental timeframes.

At 65%RH,  $\text{Cu}(\text{OH})\text{Cl}$  is the only compound identified by FTIR and Raman spectroscopy (Figure 16A,B). O-H stretching is seen at  $3456\text{ cm}^{-1}$ ,  $3384\text{ cm}^{-1}$  and  $3220\text{ cm}^{-1}$  with O-H bending at  $903\text{ cm}^{-1}$ ,  $851\text{ cm}^{-1}$  and  $805\text{ cm}^{-1}$ . Peaks at  $442\text{ cm}^{-1}$ ,  $406\text{ cm}^{-1}$  and  $398\text{ cm}^{-1}$  are associated with the Cu lattice modes as in the unexposed samples, although their relative intensity is more significant. Raman spectroscopy confirmed the FTIR identification, with characteristic peaks at O-H stretching at  $3374\text{ cm}^{-1}$ , O-H bending at  $899\text{ cm}^{-1}$ ,  $856\text{ cm}^{-1}$  and  $803\text{ cm}^{-1}$  and diagnostic lattice modes at  $480\text{ cm}^{-1}$ ,  $391\text{ cm}^{-1}$ ,  $322\text{ cm}^{-1}$ ,  $245\text{ cm}^{-1}$ ,  $184\text{ cm}^{-1}$ ,  $124\text{ cm}^{-1}$ ,  $105\text{ cm}^{-1}$ ,  $88\text{ cm}^{-1}$  and  $72\text{ cm}^{-1}$  [64].

Samples  $\geq 70\%$ RH indicate that combinations of  $\beta$ - $\text{Cu}_2(\text{OH})_3\text{Cl}$  and  $\text{CuCl}_2 \cdot 2\text{H}_2\text{O}$  (mineral name eriochalcite) are predominantly formed. The latter, when desiccated, is evident as  $\text{CuCl}_2$  (mineral name tolbacite) (Figure 17 (A–G)). Peaks suggesting the presence of  $\beta$ - $\text{Cu}_2(\text{OH})_3\text{Cl}$  are O-H stretching around  $3322\text{ cm}^{-1}$  and Cu-O-H stretches at  $986\text{ cm}^{-1}$ ,  $948\text{ cm}^{-1}$ ,  $915\text{ cm}^{-1}$ ,  $893\text{ cm}^{-1}$ ,  $849\text{ cm}^{-1}$  and  $819\text{ cm}^{-1}$  [26,66,70,71].  $\text{CuCl}_2 \cdot 2\text{H}_2\text{O}$  is evident as a broadening and shift of O-H stretches above  $3000\text{ cm}^{-1}$ , an O-H-O bending around  $1587\text{ cm}^{-1}$  and Cu-O stretch at  $680\text{ cm}^{-1}$  [72–74]. The presence of  $\text{CuCl}_2$  was confirmed with Raman spectroscopy with Cu-Cl and Cl-Cu-Cl stretching at  $98\text{ cm}^{-1}$ ,  $168\text{ cm}^{-1}$  and  $283\text{ cm}^{-1}$  (Figure 17 (G)) [75].

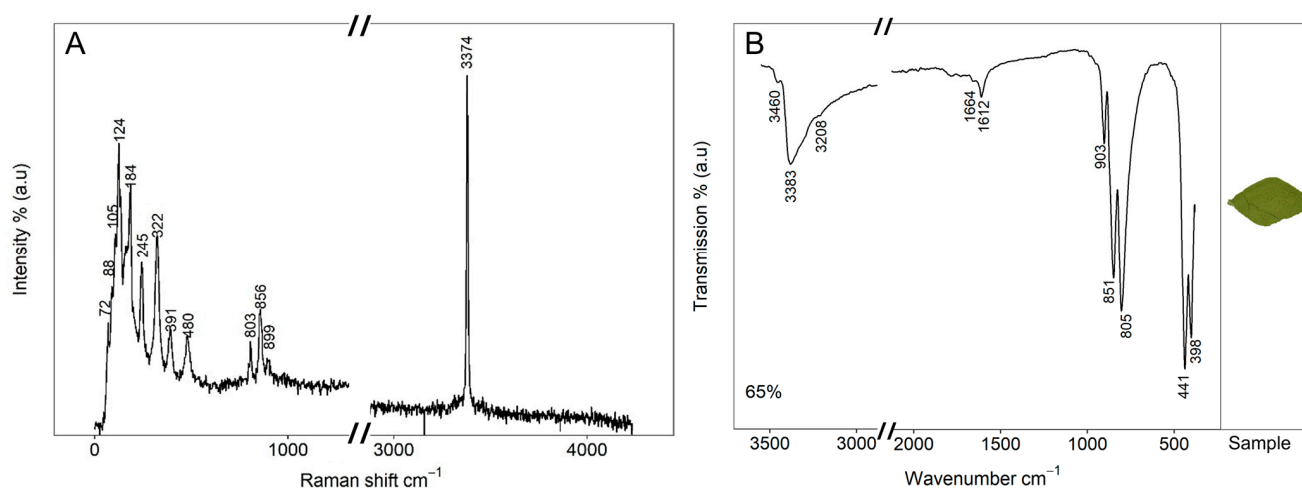


**Figure 16.** Representative CuCl samples at 65%RH and 20 °C showing the presence of Cu(OH)Cl. (A) Raman and (B) FTIR spectra. Refer to Table 2 for experimental timeframes.

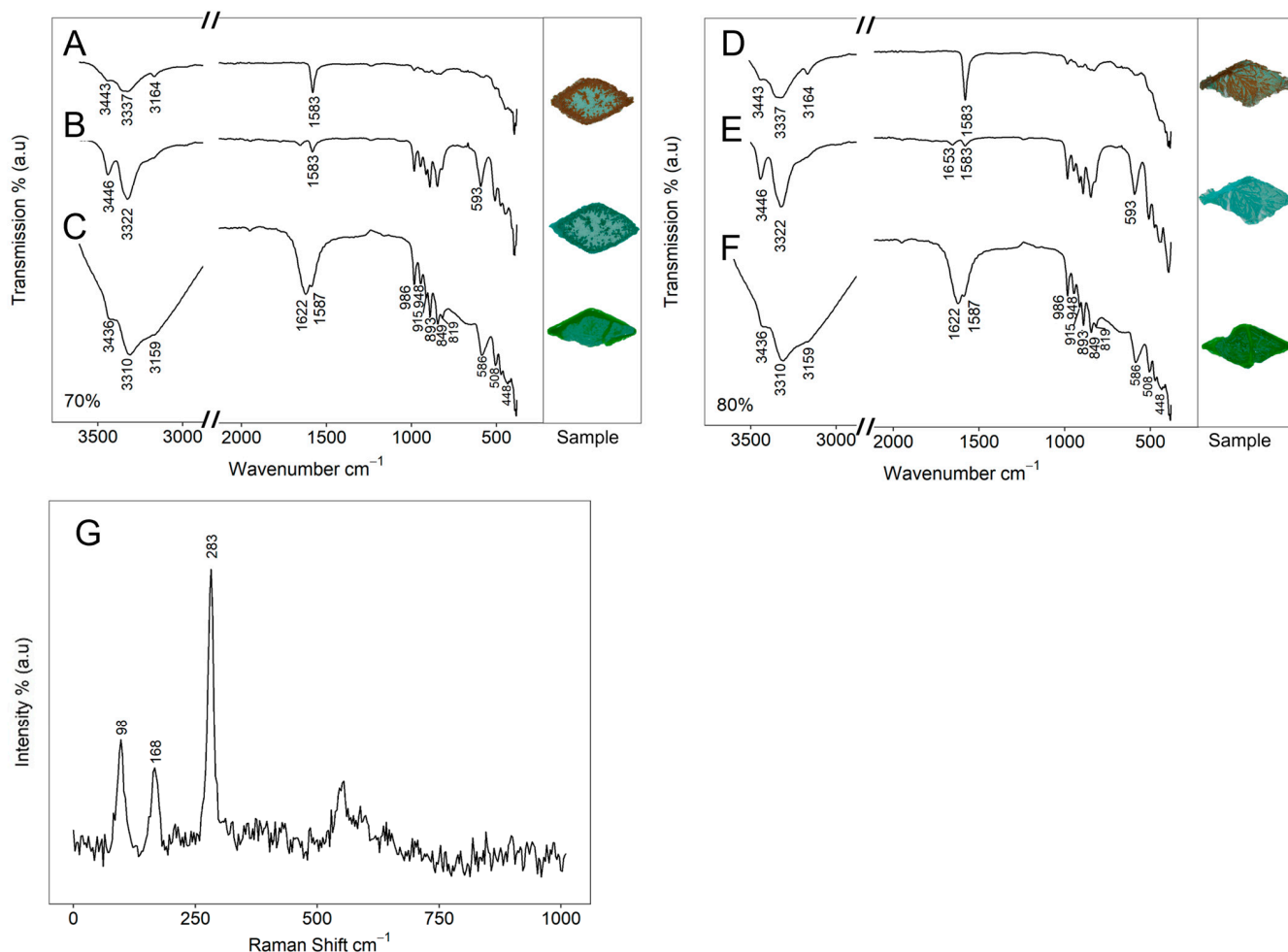


**Figure 17.** Representative CuCl samples between 70%RH and 80%RH and 20 °C, showing a mixture of  $\beta\text{-Cu}_2(\text{OH})_3\text{Cl}$  and  $\text{CuCl}_2 \cdot 2\text{H}_2\text{O}$  or  $\text{CuCl}_2$  depending on how sample has been stored. Seventy percent RH when (A) desiccated, (B) in ambient environment and (C) immediately after removal from vessel. Eighty percent RH when (D) desiccated, (E) in ambient environment and (F) immediately after removal from vessel. The locations of Cu-O-H stretches between 986  $\text{cm}^{-1}$  and 819  $\text{cm}^{-1}$  are the same in all samples and have therefore only been labelled once. (G) Raman spectra of  $\text{CuCl}_2$  crystals seen in A,D. Refer to Table 2 for experimental timeframes.

### 5.6. Cu:CuCl

All samples of CuCl mixed with copper demonstrated some structural change. At 15%RH and 153 days, O-H stretches above  $3000\text{ cm}^{-1}$  being shifted to lower wavenumbers and the appearance of new O-H bending modes can be seen at  $986\text{ cm}^{-1}$ . Cu-O-H and O-Cu-O symmetric stretching is evident at  $587\text{ cm}^{-1}$  and  $515\text{ cm}^{-1}$  (Figure 18).

$\text{Cu}_2(\text{OH})_3\text{Cl}$  compounds form in all samples containing copper  $\geq 20\%$  RH, with the ratio Cu:CuCl having no apparent impact on the nature of the compounds formed. Below 70%RH, a mixture of  $\gamma\text{-Cu}_2(\text{OH})_3\text{Cl}$  and  $\beta\text{-Cu}_2(\text{OH})_3\text{Cl}$  is evident (Figure 19 (A–P)). At and above 70%RH,  $\gamma\text{-Cu}_2(\text{OH})_3\text{Cl}$  is the only phase present (Figure 19 (Q–V)).  $\gamma\text{-Cu}_2(\text{OH})_3\text{Cl}$  is evident via O-H stretching at  $3444\text{ cm}^{-1}$ ,  $3355\text{ cm}^{-1}$  and  $3310\text{ cm}^{-1}$  with a shoulder around  $3170\text{ cm}^{-1}$ , Cu-O-H stretching at  $985\text{ cm}^{-1}$ ,  $920\text{ cm}^{-1}$ ,  $894\text{ cm}^{-1}$  (shoulder),  $860\text{ cm}^{-1}$  and  $827\text{ cm}^{-1}$ , Cu-O-H stretch at  $581\text{ cm}^{-1}$  and O-Cu-O stretch at  $510\text{ cm}^{-1}$  and Cu-Cl stretches at  $450, 402$  and  $397\text{ cm}^{-1}$ . Presence of  $\beta\text{-Cu}_2(\text{OH})_3\text{Cl}$  is evident as Cu-O-H shoulders present at  $945\text{ cm}^{-1}$  and  $848\text{ cm}^{-1}$  (Figure 19 (A–P)) [26,66,70,71]. In all samples, a weak peak around  $1241\text{ cm}^{-1}$  is associated with O-H-O stretching from water [69].

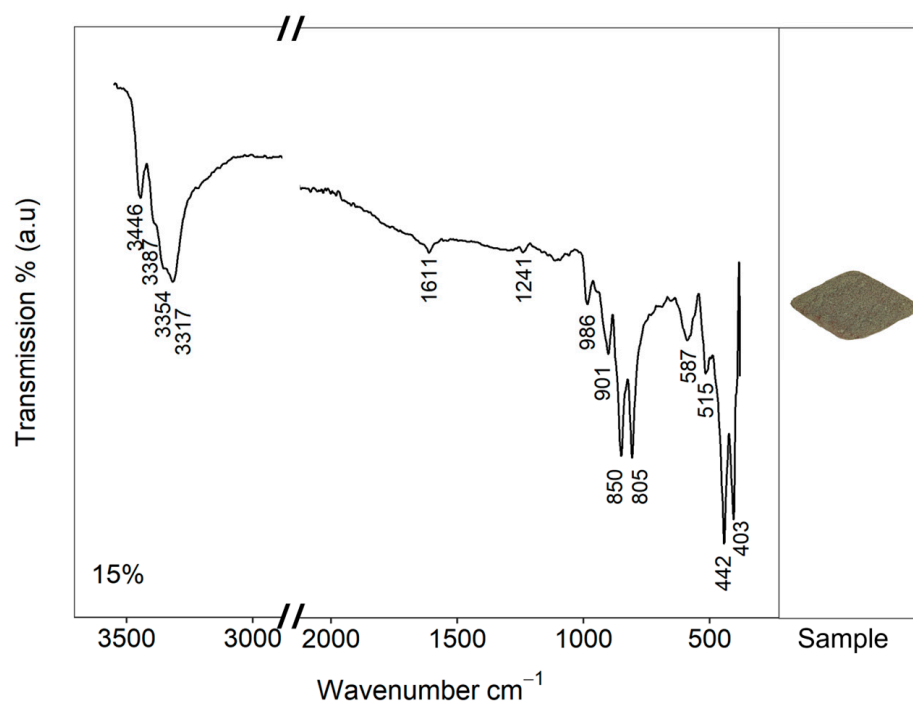


**Figure 18.** Representative FTIR spectrum of Cu:CuCl 1:1 after exposure to 15%RH and  $20\text{ }^{\circ}\text{C}$ , showing altered CuCl/Cu(OH)Cl compound. Refer to Table 2 for experimental timeframe.

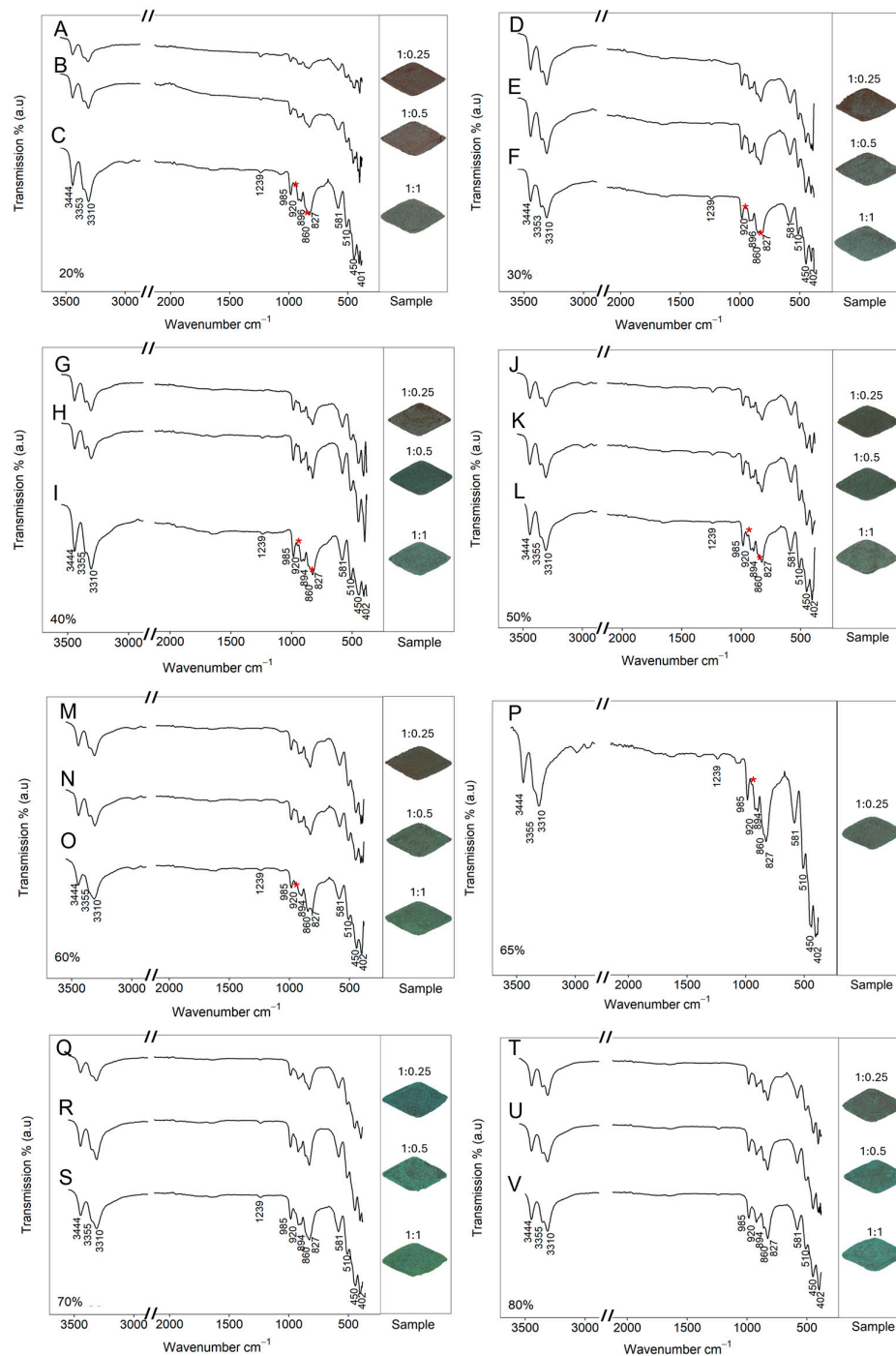


**Figure 19.** Representative FTIR spectrum of Cu:CuCl between 20–80%RH at 20 °C. Samples showing a mixture of  $\gamma$ -Cu<sub>2</sub>(OH)<sub>3</sub>Cl and  $\beta$ -Cu<sub>2</sub>(OH)<sub>3</sub>Cl after exposure to 20%RH (A–C), 30% (D–F), 40%RH (G–I), 50%RH (J–L), 60%RH, (M–O) and 65%RH (P). The presence of an asterisk indicates the location of  $\beta$ -Cu<sub>2</sub>(OH)<sub>3</sub>Cl peaks. Samples showing  $\gamma$ -Cu<sub>2</sub>(OH)<sub>3</sub>Cl after exposure to 70%RH (Q–S) and 80%RH (T–V). Diagnostic peak locations are the same within an RH group, irrespective of Cu:CuCl ratio, and have therefore only been labelled once. Refer to Table 2 for experimental timeframes.

## 6. Discussion

The results of this study reaffirm and improve the theoretical understanding of bronze disease and provide novel insights into how selected intrinsic and extrinsic variables affect its mechanisms and how kinetics can be applied to management practices for safeguarding collections.



### 6.1. Mechanisms of Bronze Disease

Oxygen consumption is measurable for samples both with and without copper powder, demonstrating that hydrolysis and oxidation of CuCl occurs without the presence of metallic copper. Since the term “bronze disease” refers to the formation of  $\text{Cu}_2(\text{OH})_3\text{Cl}$  [16], the results here are a reminder that mineralised objects containing CuCl remain at risk of bronze disease. This challenges a common conception that a metal core is required for bronze disease to occur.

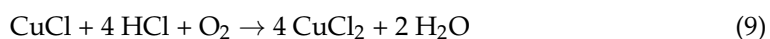
Importantly, copper not only facilitates the formation of CuCl by reacting with the byproducts of  $\text{Cu}_2(\text{OH})_3\text{Cl}$  after crystallisation but also appears to lower the critical RH threshold for hydrolysis and oxidation of CuCl. When CuCl is mixed with copper, the lowest RH at which  $\text{Cu}_2(\text{OH})_3\text{Cl}$  is detected is 20%RH, compared with 50%RH where copper is not present. These thresholds must be applied with caution, as alteration of CuCl is evident at lower RH in this study (Table 4). These changes may precede nucleation of  $\text{Cu}_2(\text{OH})_3\text{Cl}$ . These values join those produced by other studies [16,18,22,57,76] but may be the closest results yet produced to defined absolute critical thresholds.

The stoichiometries of the bronze disease reactions are well known, but less is understood about initiation of the reactions and the criteria for nucleation of  $\text{Cu}_2(\text{OH})_3\text{Cl}$  to occur. Through these FTIR and Raman spectroscopy results, coupled with oxygen consumption measurements, it is suggested that absorption of water and oxygen into the CuCl (and Cu(OH)Cl) structures occurs before nucleation of  $\text{Cu}_2(\text{OH})_3\text{Cl}$  polymorphs. Whilst water absorption is not recorded through the oxygen consumption method, the formation of the metal–oxide bond is reflected in the oxygen consumption, demonstrating why oxygen consumption occurred without the presence of  $\text{Cu}_2(\text{OH})_3\text{Cl}$  polymorphs. Water absorption followed by oxidation has been proposed as a criterion for formation of  $\text{Cu}_2(\text{OH})_3\text{Cl}$  [77], but long-term experiments are underway to establish whether the observed phenomenon is the route to bronze disease or whether insufficient moisture is present to overcome the nucleation barrier for  $\text{Cu}_2(\text{OH})_3\text{Cl}$  below 50%RH where copper is not present and below 20%RH when copper is present. Anecdotally, practitioners note that objects may show no signs of corrosion for prolonged periods before evidence of bronze disease is found [34]. This could be the time taken for sufficient water absorption to occur.

The variation in OCR over time within a given sample may reveal information about the mechanisms of bronze disease. If a first phase reflects the nucleation of  $\text{Cu}_2(\text{OH})_3\text{Cl}$ , subsequent recrystallisation of  $\text{Cu}_2(\text{OH})_3\text{Cl}$  polymorphs by the development of more energetically favoured compounds via formation of metastable phases is a possible explanation for the changes in kinetics, before OCR assumes a steady state.  $\text{Cu}_2(\text{OH})_3\text{Cl}$  polymorphs have been shown to follow the Ostwald step rules and Goldsmith’s simplicity principle, but whether the recrystallisation of these compounds from CuCl has different kinetic behaviour is unexplored [24,25,31]. A study investigating this effect is underway, but initial examination suggests that there is such a relationship between OCR and recrystallisation.

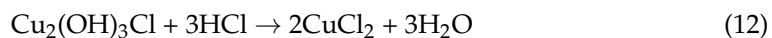
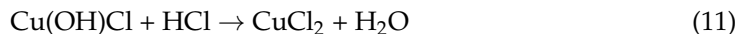
The various reactions and final products formed in this study appear to relate to both intrinsic and extrinsic variables. In all samples where copper is present, the predominant polymorph is  $\gamma\text{-Cu}_2(\text{OH})_3\text{Cl}$ , but with some  $\beta\text{-Cu}_2(\text{OH})_3\text{Cl}$  present in RH environments up to 70%RH. Increasing  $\text{Cu}^{2+}$  concentrations has been shown to promote formation of  $\gamma\text{-Cu}_2(\text{OH})_3\text{Cl}$  and is true for all Cu:CuCl ratios examined in this study [25,78].

Formation of  $\text{Cu}_2(\text{OH})_3\text{Cl}$  is accompanied by the accumulation of  $\text{Cl}^-$  in samples where no copper metal is present. This allows the formation of higher copper chloride species, such as  $\text{CuCl}_2$  [23] and  $\text{CuCl}_2 \cdot 2\text{H}_2\text{O}$ . Possible routes include the following [79]:





Formation of  $\text{CuCl}_2$  is theoretically also possible via decomposition of  $\text{Cu(OH)Cl}$  or  $\text{Cu}_2(\text{OH})_3\text{Cl}$ :



At sufficient water vapour pressure, anhydrous  $\text{CuCl}_2$  can form its dihydrate  $\text{CuCl}_2 \cdot 2\text{H}_2\text{O}$  [80].



In this study, identification of higher copper chloride species was only made in samples that contain  $\text{CuCl}$  without copper metal, suggesting that the formation of these compounds is only possible through the formation of  $\text{Cu}_2(\text{OH})_3\text{Cl}$  and where there are no  $\text{Cu}^+$  ions to counteract the accumulation of  $\text{Cl}^-$ . Copper metal may also affect the dominant polymorph formed.  $\beta\text{-Cu}_2(\text{OH})_3\text{Cl}$  is the predominant product in  $\text{CuCl}$  samples where no copper is present and at higher RH is the only polymorph identified. This agrees with studies reporting that the absence of copper, or low  $\text{Cu}^+$  concentrations, yield a longer period during which  $\beta\text{-Cu}_2(\text{OH})_3\text{Cl}$  is the stable polymorph [25,26] and that high concentration of  $\text{Cl}^-$  (above  $0.06 \text{ mol/dm}^{-3}$ ) can favour the formation of atacamite [25,31].

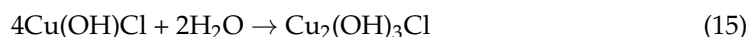
The results of this study bring into question the possible role of  $\text{Cu(OH)Cl}$  in bronze disease.  $\text{Cu(OH)Cl}$  is not traditionally considered in bronze disease mechanisms and has not been identified as a product on archaeological objects, probably due to its instability. However, it is a naturally occurring compound [65], and its presence has been recorded when simulating the formation of  $\text{Cu}_2(\text{OH})_3\text{Cl}$  via  $\text{CuCl}$  [57,81,82] and  $\text{CuCl}_2$  [26,27,66,83]. Therefore, it should be considered a theoretically possible part of bronze disease routes. Limited quantification of crystalline phases has revealed that it develops during the corrosion process, decomposing into  $\text{Cu}_2(\text{OH})_3\text{Cl}$  polymorphs [57,82], indicating that it potentially plays a more important role than just as a contaminant of  $\text{CuCl}$  during synthesis.

Results here suggest that there are conditions in which  $\text{Cu(OH)Cl}$  is the preferred compound, as evident in samples at 65%RH. The reason for the occurrence of  $\text{Cu(OH)Cl}$  in the context of  $\text{CuCl}$  must be examined in more detail. Formation of  $\text{Cu(OH)Cl}$  may require fewer molecules of water than  $\text{Cu}_2(\text{OH})_3\text{Cl}$  and may not produce any other ionic species or compounds during its formation. A stoichiometrically possible reaction may be the following:



although the thermodynamics of this must be examined.

Rapid decomposition of both naturally occurring and synthetic  $\text{Cu(OH)Cl}$  to  $\text{Cu}_2(\text{OH})_3\text{Cl}$  polymorphs is acknowledged [26,65,66,84] but not in the context of bronze disease. A lack of symmetry in  $\text{Cu(OH)Cl}$  has been proposed to be responsible for its instability [85], and it is assumed that further absorption of moisture results in its decomposition to  $\text{Cu}_2(\text{OH})_3\text{Cl}$  [86]:



Finally, the cyclical aspect of bronze disease when  $\text{CuCl}$  is mixed with copper has been illustrated. No reaction endpoint was identified where copper was present in samples, confirming that the release of  $\text{HCl}$  or dissolved  $\text{H}^+$  and  $\text{Cl}^-$  from the formation of  $\text{Cu}_2(\text{OH})_3\text{Cl}$  reacts with  $\text{Cu}^+$  ions to continuously form more  $\text{CuCl}$  [23]. The endpoint of oxygen consumption with  $\text{CuCl}$  alone confirms that bronze disease ceases where there is no more  $\text{CuCl}$  left to react.

## 6.2. Kinetics of Bronze Disease

The kinetics of bronze disease for an object can be affected by a range of intrinsic and extrinsic factors.

### 6.2.1. Intrinsic

The presence of metallic copper affects both mechanisms and kinetics of bronze disease. When CuCl is mixed with copper, formation of  $\text{Cu}_2(\text{OH})_3\text{Cl}$  is more significant between 20 and 60%RH, suggesting that copper has a catalytic effect on oxidation and hydrolysis of CuCl and that dissolved  $\text{Cu}^{2+}$  and  $\text{Cu}^+$  ions may have the capacity to lower the activation energy for CuCl transformation to  $\text{Cu}_2(\text{OH})_3\text{Cl}$ . An excess of  $\text{Cu}^{2+}$  ions have been noted to promote the transformation of  $\text{Cu}_2(\text{OH})_3\text{Cl}$  polymorphs during synthesis [25]. By allowing the continuous formation of CuCl, copper is also thought to contribute to a faster OCR, as there are more sites for nucleation of  $\text{Cu}_2(\text{OH})_3\text{Cl}$  at any time in comparison to a depleting amount of CuCl when copper is not present. Formation of  $\text{Cu}_2\text{O}$  through oxidation of copper is possible but is not considered a contributing factor in the accelerating trends. In the environments tested in this study, formation of  $\text{Cu}_2\text{O}$  is not the thermodynamically favoured reaction [16,87], and the oxidation of copper control samples occurs at an appreciably slower rate than samples containing CuCl, showing that the contribution to the overall OCR is negligible. The phenomenon of CuCl hydrolysing to  $\text{Cu}_2(\text{OH})_3\text{Cl}$  at a slower rate than Cu:CuCl mixtures up to 65%RH and faster above this threshold has been noted in short experimental studies over a limited range of RH [57,82], but the role of Cu in this process and the possible reasons behind this have not been explored in detail.

Varying the relative ratio of copper to CuCl in this study had multiple effects. In any given environment, the OCR increases with increasing CuCl, as there are more opportunities for nucleation of  $\text{Cu}_2(\text{OH})_3\text{Cl}$  and, consequently, for more CuCl to form. In contrast, the effect of changing RH, either incrementally or cumulatively, is more significant where the ratio of CuCl to copper is smaller, which could be an effect of higher  $\text{Cu}^+$  ratios. However, the ratios and amounts of Cu:CuCl examined here all have similar exponential increases in OCR with a rise in RH, showing that it is the presence of copper that has the most significant impact on the hydrolysis and oxidation of CuCl.

When  $\text{CuCl}_2$  and  $\text{CuCl}_2 \cdot \text{H}_2\text{O}$  exist in corrosion profiles, there are implications for the kinetics of bronze disease. This is particularly evident in CuCl samples in environments  $\geq 70\%RH$ . As these compounds do not generally require oxygen to form (with the possible exception of reaction (10)), their formation would not be recorded using oxygen consumption, and it is assumed that these compounds accelerate the formation of  $\text{Cu}_2(\text{OH})_3\text{Cl}$ . Being hygroscopic and water-soluble, they are thought to facilitate hydration of ions, thereby lowering critical thresholds for reaction [87]. Alongside formation of  $\text{CuCl}_2$  and  $\text{CuCl}_2 \cdot 2\text{H}_2\text{O}$ , accumulation of  $\text{Cl}^-$  or HCl can accelerate corrosion rates by lowering the overall pH of a solution formed in samples  $\geq 70\%RH$  [8].

### 6.2.2. Extrinsic

Altering the RH at a static temperature influences OCR across all samples and the rate at which  $\text{Cu}_2(\text{OH})_3\text{Cl}$  polymorphs are formed. The exponential acceleration of OCR with RH in all samples is similar to those measured on clean metal surfaces [88–91] and aligns well with results of a similar experiment that examined the formation of  $\text{Cu}_2(\text{OH})_3\text{Cl}$  in different RH environments [22]. It is suggested that increasing RH increases the adsorbed monolayers of waters and absorbed water in the crystal lattice, facilitating the precipitation of  $\text{Cu}_2(\text{OH})_3\text{Cl}$  polymorphs. A critical threshold of acceleration is evident around 65–70%RH, where the adsorbed water is said to take on the properties of bulk water [54]. Availability of water is a critical parameter of bronze disease, not only as an electrolyte but

also to allow absorption of water into the CuCl structure. The relationship of increasing water availability causing increasing nucleation and crystallisation of  $\text{Cu}_2(\text{OH})_3\text{Cl}$  is evident here and can be quantified. The samples measured in this study are exposed to different RH conditions at a static temperature (20 °C), but temperature has also been shown to affect the rate at which bronze disease occurs in accordance with the Arrhenius equation, which must be considered when estimating risk to objects [60].

### 6.3. Endpoint for Bronze Disease

Rates of bronze disease are expected to decrease over time due to multiple factors. Continuous formation of  $\text{Cu}_2(\text{OH})_3\text{Cl}$  will decrease transport of dissolved oxygen. Diminishing CuCl will decrease the number of sites at which reactions can occur. Where copper ions are present, depletion of copper by continuous formation of CuCl will eventually affect the rate of formation of CuCl and  $\text{Cu}_2(\text{OH})_3\text{Cl}$ .

### 6.4. Practical Implications

Understanding the oxidation and hydrolysis of CuCl as a function of relative humidity allows formulation of evidence-based recommendations for practice. The limitations of replicating complex relationships between alloying elements, such as Sn and Zn, and corrosion profiles are acknowledged and should be subject to further study.

Bronze disease can occur in all objects containing CuCl, but its rate is likely to be more rapid in environments below 60%RH for objects containing a metal core than without. In objects without a metallic core and with CuCl in isolation, the development of bronze disease is likely to be very slow until formation of soluble CuCl species occurs around 50%RH, which accelerates the rate at which  $\text{Cu}_2(\text{OH})_3\text{Cl}$  is formed. Examining oxygen consumption rates and quantifying how the risk changes incrementally or cumulatively can indicate how risk changes across a range of RH environments (Figure 20). Classification of risk into simple low-medium-high categories can also be attempted (Figure 21).

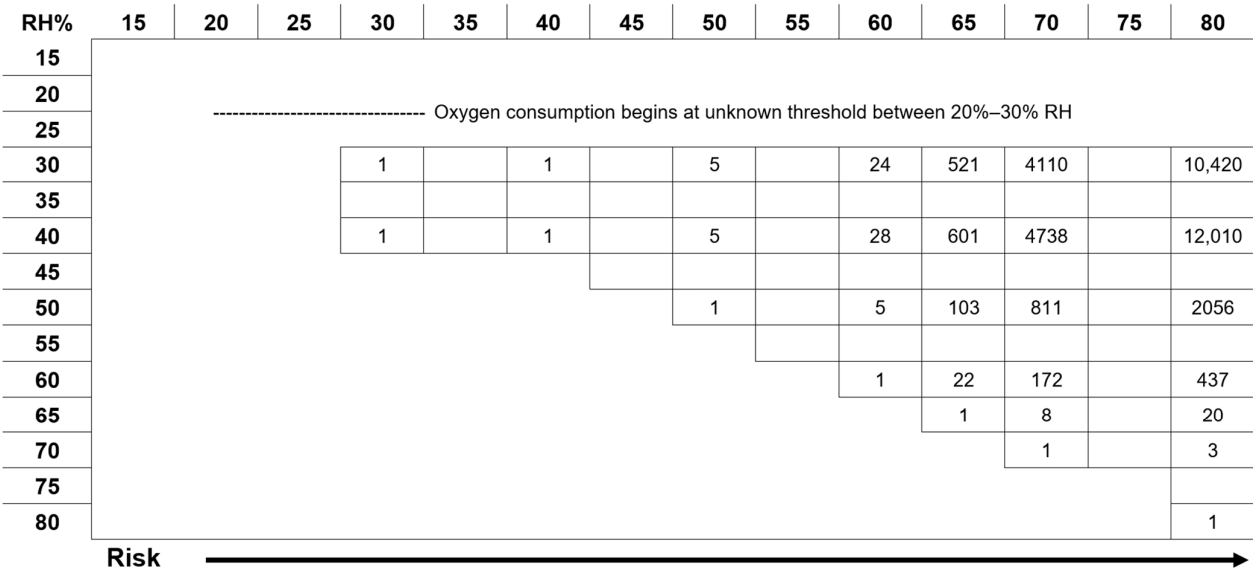
The identification of CuCl alteration and formation of  $\text{Cu}_2(\text{OH})_3\text{Cl}$  at a lower RH threshold than previously measured prompts further questions about critical thresholds. Attempting to achieve low RH values for storage and display of copper alloy objects where there is no risk of CuCl alteration is wasteful of resources and may not always be feasible [49,59]. Understanding how risk escalates either incrementally or over larger RH ranges can allow flexibility in management goals. If some risk is acceptable, environmental targets can be relaxed. Arguably, the acceleration of bronze disease between 60 and 70%RH is the most critical threshold to adhere to. Significant risk to objects must be expected between and above these values. Although overall corrosion rates can be expected to differ, the acceleration of risk with RH, in particular the acceleration around 60%RH, aligns with thresholds identified for archaeological iron [48]. RH thresholds should be considered alongside the temperature of a collection environment, which has been shown to affect corrosion rates where the humidity is static [60].

When a metallic core is present, the bronze disease process is likely to continue until all metallic copper is consumed and will have a detrimental effect on the object. In a mineralised object, bronze disease will continue until all CuCl has been transformed. Whilst it is difficult to identify and quantify CuCl within corrosion profiles, the identification of a metallic core can prove a helpful estimate of the likelihood of bronze disease and the magnitude of the damage it might cause.

If a green acidic liquid [15,18] is present or staining has occurred on the packaging surrounding an object, this may be  $\text{CuCl}_2(\text{aq})$  and can indicate that CuCl is present within the corrosion profile and that the object has a past history of being subjected to high RH environments. Objects that have been stored in enclosed environments, such as small

crystal boxes or failed desiccated microclimates, may be more prone to this. When detected, both anhydrous and dihydrate forms of CuCl<sub>2</sub> should be removed, as this can accelerate bronze disease. Noting CuCl<sub>2</sub> or CuCl<sub>2</sub>·2H<sub>2</sub>O as part of the corrosion profile is unusual, but not unheard of [30,32,92,93].

CuCl



CuCl, copper

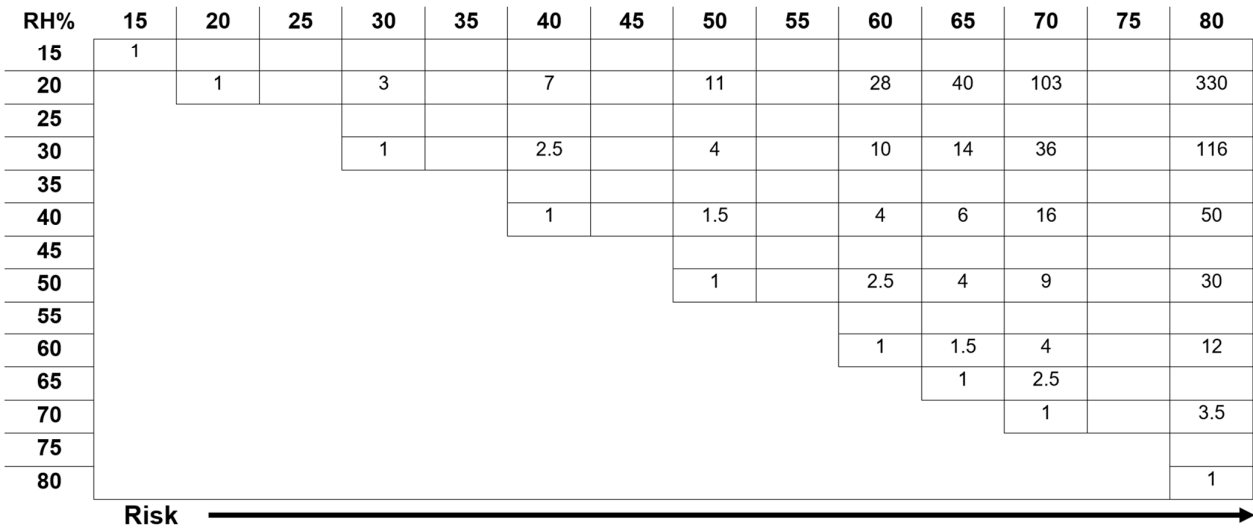


Figure 20. Matrix indicating how risk, presented as the factor increase of measured OCR, changes with RH. Y-axis is the initial RH, and X-axis is the elevated RH. Data for CuCl (above) and CuCl in contact with copper (below). Factors are rounded to the nearest 0.5 if value is <10.

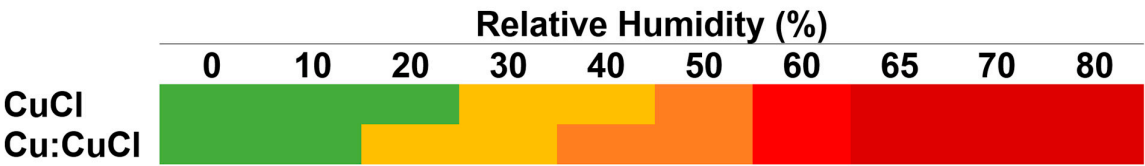


Figure 21. Indicative risk scale from none (green), low (yellow), medium (orange) and high (bright red) to very high (dark red) with measured accelerating factor from 30%RH (CuCl) and 20%RH (Cu:CuCl 1:0.25).

The experimental protocol used in this study has isolated the oxidative hydrolysis reaction of CuCl, but it is acknowledged that the oxygen consumption rates here cannot predict when bronze disease will become detectable on an object and when, where and to what extent damage will occur, due to the many rate-influencing factors caused by the corrosion profiles of objects that cannot be replicated. The experimental setup was designed to facilitate measurable oxygen consumption by combining large sample sizes in relation to the volume of gas within the oxygen vessel [62,94]. The combination of the large surface areas of the powders used and ready access to both oxygen and atmospheric water is unlikely to occur in objects with complex corrosion profiles. In objects, the properties of different corrosion compounds, their thicknesses, adhesion and coherence can facilitate or hinder ionic transport necessary to initiate bronze disease. The correlation between RH and monolayers becomes more complex as porous products can retain water within the structure [33,95,96] with smaller capillaries permitting condensation of water at lower RH; for example, condensation can occur at 50%RH for capillaries of 1.5 nm as compared to 98%RH for 36 nm [97]. As seen in this study, the presence of hygroscopic compounds on the surface of the object can also alter critical relative humidity levels. Rates are further likely to vary in archaeological objects depending on where CuCl is located and where damage caused by formation of  $\text{Cu}_2(\text{OH})_3\text{Cl}$  occurs and to what extent. Over time, as  $\text{Cu}_2(\text{OH})_3\text{Cl}$  forms, damage to a patina may allow access to oxygen and water more readily, increasing the rate of formation. If the products from the reaction form and block channels and pores in the patina, rates may subsequently become slower. Major and minor alloying elements may change the thermodynamic tendencies and kinetics for some of the reactions considered, but comparative studies are limited [16]. All of the factors considered above contribute to the unpredictability of bronze disease in archaeological copper alloy objects and highlight the need for continued research within this field. By focusing on the fundamental reactions of bronze disease, it is believed that the results are applicable to objects of different compositions and corrosion profiles.

## 7. Conclusions

For the first time, the implications of the presence of metallic copper on the rate at which hydrolysis and oxidation of CuCl occurs and which compounds form have been demonstrated. This evidences that not only is copper responsible for the cyclic aspect of bronze disease but its presence has other management complications. Additionally, experiments have offered further insight into the kinetics of the “bronze disease” phenomenon occurring on copper alloys. This has facilitated the development of risk assessment advice for the heritage sector, which can improve conservation practice and longevity of archaeological copper alloy heritage.

Tangible guidance for best practice preservation of archaeological copper alloys, based on the results of this study, includes the following:

- Where possible, establish whether objects have a metallic core, using, e.g., X-radiography. This will form the basis for management protocols.
- Use the charts provided to determine acceptable risk. Retain objects below 20%RH if any formation of  $\text{Cu}_2(\text{OH})_3\text{Cl}$  is unacceptable. Risk is low for objects with no copper core up to 50%RH and low up to 40%RH for objects with a copper core.
- Maintaining environments up to 60%RH for displaying mixed materials will promote bronze disease in objects with a metal core at a more rapid rate than mineralised objects.
- The formation of soluble chloride compounds in uncontrolled, enclosed environments can accelerate bronze disease, especially if objects have no metal core.
- During monitoring, check for surrounding green staining on packaging. This can indicate the presence of soluble chloride compounds and current or prior incorrect storage.



- Perform regular monitoring and maintenance of any environmental control system, e.g., desiccated microclimates [98]. Adjust the use of desiccant to manipulate RH threshold and maintenance intervals [48,99].
- Fluctuating environments where soluble compounds can deliquesce and crystallise may cause additional irreversible damage. If possible, identify and remove water-soluble compounds.

The work carried out here complements and fills the gap to evidence and extend the efficacy of existing guidance, which, hitherto, relied upon limited research, anecdote and experience.

**Author Contributions:** Conceptualization, J.T., N.E. and D.W.; methodology, J.T., N.E. and D.W.; formal analysis, J.T.; investigation, J.T.; data curation, J.T.; writing—original draft preparation, J.T.; writing—review and editing, N.E. and D.W.; visualization, J.T.; supervision, N.E. and D.W.; funding acquisition, J.T., N.E. and D.W. All authors have read and agreed to the published version of the manuscript.

**Funding:** This research was funded by the Arts and Humanities Research Council, South, West and Wales Doctoral Training Partnership Studentship.

**Data Availability Statement:** The datasets presented in this article are not readily available because the data is part of an ongoing study. Requests to access the datasets should be directed to J.T.

**Conflicts of Interest:** The authors declare no conflicts of interest.

## References

- Watkinson, D. Conservation Science in Practice. In *Handbook of Archaeological Sciences*, 2nd ed.; Pollard, A.M., Armitage, R.A., Makarewicz, C.A., Eds.; John Wiley and Sons: Hoboken, NJ, USA, 2023; pp. 1063–1073.
- Robbiola, L.; Blengino, J.M.; Fiaud, C. Morphology and mechanisms of formation of natural patinas on archaeological Cu-Sn alloys. *Corros. Sci.* **1998**, *40*, 2083–2111. [[CrossRef](#)]
- Bertholon, R. Archaeological metal artefacts and conservation issues: Long-term corrosion studies. In *Corrosion of Metallic Heritage Artefacts. Investigation, Conservation and Prediction of Long Term Behaviour*; Dillman, P., Béranger, G., Piccardo, P., Matthiesen, H., Eds.; European Federation of Corrosion (EFC) Series Number 48; Woodhead Publishing in Materials: Cambridge, UK, 2007; pp. 31–40.
- Nord, A.G.; Mattsson, E.; Tronner, K. Factors Influencing the Long-term Corrosion of Bronze Artefacts in Soil. *Prot. Met.* **2005**, *41*, 309–319. [[CrossRef](#)]
- Oudbashi, O. A methodological approach to estimate soil corrosivity for archaeological copper alloy artefacts. *Herit. Sci.* **2018**, *6*, 1–15. [[CrossRef](#)]
- Di Turo, F.; Coletti, F.; De Vito, C. Investigations on alloy-burial environment interaction of archaeological bronze coins. *Microchem. J.* **2020**, *157*, 104882. [[CrossRef](#)]
- McNeil, M.B. Interpretation of Bronze Disease and Related Copper Corrosion Mechanisms in Terms of Log-Activity Diagrams. *Mater. Res. Soc. Symp. Proc.* **1992**, *267*, 1055–1106. [[CrossRef](#)]
- Wang, J.; Xu, C.; Lv, G. Formation processes of CuCl and regenerated Cu crystals on bronze surfaces in neutral and acidic media. *Appl. Surf. Sci.* **2006**, *252*, 6294–6303. [[CrossRef](#)]
- Fan, Z.; Zhou, H.; Wang, X.; Song, H.; Shi, J.; Chen, J. Comparison and study of the corrosion differences of bronze alloys in oxygen-free and oxygen-containing conditions. *Corros. Sci.* **2024**, *241*, 112553. [[CrossRef](#)]
- Payer, J.H.; Ball, G.; Rickett, B.I.; Kim, H.S. Role of transport properties in corrosion product growth. *Mater. Sci. Eng. A* **1995**, *198*, 91–102. [[CrossRef](#)]
- Constantinides, I.; Adriaens, A.; Adams, F. Surface characterization of artificial corrosion layers on copper alloy reference materials. *Appl. Surf. Sci.* **2002**, *189*, 90–101. [[CrossRef](#)]
- Dowsett, M.; Adriaens, A.; Martin, C.; Bouchenoire, L. The use of synchrotron X-rays to observe copper corrosion in real time. *Anal. Chem.* **2012**, *84*, 4866–4872. [[CrossRef](#)]
- Grayburn, R.; Dowsett, M.; Hand, M.; Sabbe, P.-I.; Thompson, P.; Adriaens, A. Tracking the progression of bronze disease. *Corros. Sci.* **2015**, *91*, 220–223. [[CrossRef](#)]

14. Fischer, W.R.; Wagner, B.D.; Siedlarek, H.; Füßinger, B. The influence of chloride ions and light on the corrosion behaviour of copper alloys in aqueous environment with special regards to bronze disease. In *Metal 95. Proceedings of the International Conference on Metals Conservation, Semur en Auxois, France, 25–28 September 1995*; MacLeod, I.D., Pennec, S.L., Robbiola, L., Eds.; James & James: London, UK, 1997; pp. 89–94.
15. Scott, D.A. *Copper and Bronze in Art: Corrosion, Colorants, Conservation*; The Getty Conservation Institute: Los Angeles, CA, USA, 2002.
16. Scott, D.A. Bronze Disease: A Review of Some Chemical Problems and the Role of Relative Humidity. *J. Am. Inst. Conserv.* **1990**, *29*, 193–206. [\[CrossRef\]](#)
17. Organ, R.M. The examination and treatment of bronze antiquities. *Stud. Conserv.* **1961**, *6* (Suppl. 1), 104–110. [\[CrossRef\]](#)
18. Organ, R.M. Aspect of Bronze Patina and its Treatment. *Stud. Conserv.* **1963**, *8*, 1–9. [\[CrossRef\]](#)
19. De Ryck, I.; Pantos, E.; Adriaens, A. Near Eastern ancient bronze objects from Tell Beydar (NE-Syria): Insights into their corrosion. *Europhys. News* **2007**, *38*, 29–33. [\[CrossRef\]](#)
20. Giovanelli, G.; D’Urzo, L.; Maggiulli, G.; Natali, S.; Pagliara, C.; Sgura, I.; Bozzini, B. Cathodic chloride extraction treatment of a late Bronze Age artifact affected by bronze disease in room-temperature ionic-liquid 1-ethyl-3-methylimidazolium bis(trifluoromethanesulfonyl)imide (EMI-TFSI). *J. Solid State Electrochem.* **2010**, *14*, 479–494. [\[CrossRef\]](#)
21. Oudbashi, O.; Mohammadamin Emami, S.; Ahmadi, H.; Davami, P. Micro-stratigraphical investigation on corrosion layers in ancient Bronze artefacts by scanning electron microscopy energy dispersive spectrometry and optical microscopy. *Herit. Sci.* **2013**, *1*, 21. [\[CrossRef\]](#)
22. Thickett, D. Critical Relative Humidity Levels and Carbonyl Pollution Concentrations for Archaeological Copper Alloys. In *Proceedings of the ICOM-CC Metals Working Group New Delhi 2016, New Delhi, India, 26–30 September 2016*; Menon, R., Chemello, C., Pandya, A., Eds.; International Council of Museums Committee for Conservation and Indira Gandhi National Centre for the Arts: New Delhi, India, 2016; pp. 180–187.
23. MacLeod, I. Bronze disease: An electrochemical explanation. *ICCM Bull.* **1981**, *7*, 16–26. [\[CrossRef\]](#)
24. Krivovichev, S.V.; Hawthorne, F.C.; Williams, P.A. Structural complexity and crystallisation: The Oswald sequence of phases in the  $\text{Cu}_2(\text{OH})_3\text{Cl}$  system (Botallackite-atacamite-clinoatacamite). *Struct. Chem.* **2016**, *28*, 1.
25. Pollard, A.M.; Thomas, R.G.; Williams, P.A. Synthesis and stabilities of basic copper(II) chlorides atacamite, paratacamite and botallackite. *Mineral. Mag.* **1989**, *53*, 557–563. [\[CrossRef\]](#)
26. Tennent, N.H.; Antonio, K.M. Bronze Disease: Synthesis and Characterisation of Botallackite, Paratacamite and Atacamite by Infra-Red Spectroscopy. In *Proceedings of the ICOM Committee for Conservation 6th Triennial Meeting, Metals Working Group, Ottawa, ON, Canada, 21–15 September 1981*; International Council of Museums: Paris, France, 1981; p. 81/23/3-1.
27. Sharkey, J.B.; Lewin, S.Z. Conditions governing the formation of atacamite and paratacamite. *Am. Min.* **1971**, *56*, 179–192.
28. Jambor, J.L.; Dutrizac, J.E.; Roberts, A.C.; Grice, J.D.; Szymanski, J.T. Clinoatacamite, a new polymorph of  $\text{Cu}_2(\text{OH})_3\text{Cl}$ , and its relationship to paratacamite and “anarakite”. *Can. Miner.* **1996**, *34*, 61–72.
29. Grice, J.D.; Szymanski, J.T.; Jambor, J.L. The crystal structure of clinoatacamite, a new polymorph of  $\text{Cu}_2(\text{OH})_3\text{Cl}$ . *Can. Miner.* **1996**, *34*, 73–78.
30. Scott, D.A. New insights on the corrosion of ancient bronzes using X-ray powder diffraction: The importance of paratacamite, sampleite, and connellite. *Stud. Conserv.* **2017**, *62*, 410–418. [\[CrossRef\]](#)
31. Pollard, A.M.; Thomas, R.G.; Williams, P.A. The Copper Chloride System and Corrosion: A Complex Interplay of Kinetic and Thermodynamic Factors. In *Dialogue/89: The Conservation of Bronze Sculpture in the Outdoor Environment: A Dialogue Among Conservators, Curators, Environmental Scientists, and Corrosion Engineers*; Drayman, T.S., Ed.; NACE: Houston, TX, USA, 1992; pp. 123–133.
32. Fabrizi, M.; Scott, D.A. Unusual copper corrosion products and problems of identity. In *Recent Advances in the Conservation and Analysis of Artifacts*; Black, J., Ed.; Jubilee Conservation Conference Papers; Summer School Press: London, UK, 1987; pp. 131–133.
33. MacLeod, I.D.; Näsänen, L.M.E. Evaluation of Chloride Extraction Rates from Copper Compounds Under Subcritical Conditions. *Stud. Conserv.* **2023**, *69*, 608–620. [\[CrossRef\]](#)
34. MacLeod, I.D. Conservation of Corroded Copper Alloys: A Comparison of New and Traditional Methods for Removing Chloride Ions. *Stud. Conserv.* **1987**, *32*, 25–40. [\[CrossRef\]](#)
35. Uminski, M.; Guidetti, V. The removal of chloride ions from artificially corroded bronze plates. *Stud. Conserv.* **1995**, *40*, 274–278. [\[CrossRef\]](#)
36. Golfomitsou, S.; Merkel, J.F. Synergistic effects of corrosion inhibitors for copper and copper alloy archaeological artefacts. In *Metal 04: Proceeding of the International Conference on Metals Conservation, National Museum of Australia, Canberra, Australia, 4–8 October 2004*; Ashton, J., Hallam, D., Eds.; National Museum of Australia: Canberra, ACT, Australia, 2004; pp. 344–368.
37. Abu-Baker, A.N.; Al-Qudah, M.A. A novel dioxime compound for protecting copper in neutral chloride solutions and to treat bronze disease in archaeological artefacts. *AICCM Bull.* **2017**, *38*, 94–102. [\[CrossRef\]](#)

38. Saleh, S.M.; El-Badry, A.E.H.A.; Abdel-Karim, A.M. Evaluation of the corrosion resistance of bronze patina or/and protective coating on the surface of the archaeological coins. *Sci. Rep.* **2025**, *15*, 2361. [[CrossRef](#)]
39. Madsen, B.H. A Preliminary Note on the Use of Benzotriazole for Stabilizing Bronze Objects. *Stud. Conserv.* **1967**, *12*, 163–167. [[CrossRef](#)]
40. Sease, C. Benzotriazole: A Review for Conservators. *Stud. Conserv.* **1978**, *23*, 76–85. [[CrossRef](#)]
41. Molina, T.; Cano, E.; Ramirez-Barat, B. Protective coatings for metallic heritage conservation: A review. *J. Cult. Herit.* **2023**, *62*, 99–113. [[CrossRef](#)]
42. D'Ars, F.; João Cura, J.; De Bellis, V.M.; Lins, V.M.C.; Souza, L.A.Z. A Note on the Products of the Reaction of AMT with Bronze and with Three Corrosion Products of Bronze. *Stud. Conserv.* **2007**, *52*, 147–153. [[CrossRef](#)]
43. McEnroe, K.; Lobley, I.; Kerns, A. Benzotriazole (BTA): A Review of the Current Research into Toxicity. *J. Am. Inst. Conserv.* **2025**, 1–18. [[CrossRef](#)]
44. Madsen, B. Benzotriazole: A perspective. In *Corrosion Inhibitors in Conservation*; UKIC Occasional Paper 4; UKIC: London, UK, 1985; pp. 19–20.
45. Wolfe, J.; Grayburn, R. A review of the development and testing of Incralac lacquer. *J. Am. Inst. Conserv.* **2017**, *56*, 225–244. [[CrossRef](#)]
46. Tennent, N.H. Conservation science: A view from four perspectives. In *The Interface Between Science and Conservation*; British Museum Occasional Paper; British Museum: London, UK, 1997; p. 126.
47. Boyatzis, S.C.; Veve, A.; Kriezi, G.; Karamargiou, G.; Kontou, E.; Argyropoulos, V. A Scientific Assessment of the Long-Term Protection of Incralac Coatings on Ancient Bronze Collections in the National Archaeological Museum and the Epigraphic and Numismatic Museum in Athens, Greece. In *Artistry in Bronze: The Greeks and Their Legacy XIXth International Congress on Ancient Bronzes*; Daehner, J.M., Lapatin, K., Spinelli, A., Eds.; Getty Publications: Los Angeles, CA, USA, 2017; pp. 300–312.
48. Thunberg, J.; Watkinson, D.; Emmerson, N. Desiccated microclimates for heritage metals: Creation and management. *Stud. Conserv.* **2021**, *66*, 127–153. [[CrossRef](#)]
49. Ganiaris, H.; Barham, L.; Goodman, L. Great expectations: A review of iron from waterlogged contexts from London sites excavated in the 1980s and 1990s. *J. Inst. Conserv.* **2012**, *35*, 3–13. [[CrossRef](#)]
50. Bryan, B.N. Copper alloy objects suspected of bronze disease—The Burrell ‘Bronzes’. In *Studies in Archaeological Conservation*; Caple, C., Garlick, V., Eds.; Routledge: London, UK, 2021; pp. 115–123.
51. Brown, J.P. The Field Museum archaeological metals project: Distributed, in situ microenvironments for the preservation of unstable archaeological metals using Escal barrier film. In *Objects Speciality Group Postprints*; American Institute for Conservation of Historic and Artistic Works: Washington, DC, USA, 2010; Volume 17, pp. 133–146.
52. Oudbashi, O. From Excavation to Preservation: Preventive Conservation Approaches in Archaeological Bronze Collections. In *La Conservation-Restauration des Métaux Archéologiques: Des Premiers Soins à la Conservation Durable, Proceedings of the Colloque Organisé par la Direction de l'Archéologie du Service Public de Wallonie et la DGO4, la FAW (Fédération des Archéologues de Wallonie et de Bruxelles) et le CReA-Patrimoine (ULB), Bruxelles, Belgium, 8–9 May 2014*; L'Université Libre de Bruxelles: Bruxelles, Belgium, 2015; pp. 29–35.
53. Leygraf, C.; Graedel, T. *Atmospheric Corrosion*; Wiley: Chichester, UK, 2000.
54. Jones, D.A. *Principles and Prevention of Corrosion*; Macmillan Publishing Company: New York, NY, USA, 1991.
55. Watkinson, D.; Lewis, M.R.T. Desiccated storage of chloride-contaminated archaeological iron objects. *Stud. Conserv.* **2005**, *50*, 241–252. [[CrossRef](#)]
56. Watkinson, D.E.; Rimmer, M.B.; Emmerson, N.J. The Influence of Relative Humidity and Intrinsic Chloride on Post-excavation Corrosion Rates of Archaeological Wrought Iron. *Stud. Conserv.* **2019**, *64*, 456–471. [[CrossRef](#)]
57. Papapelekanos, A. The Critical RH for the Appearance of “Bronze Disease” in Chloride Contaminated Copper and Copper Alloy Artefacts. *E-Conserv. Mag.* **2010**, *13*, 43–51.
58. Thickett, D.; Mélinis, A.; Shah, B. Measurement of Sorption Isotherms to Guide Mixed Display of Archaeological Iron, Bone and Glass. *Materials* **2024**, *17*, 5934. [[CrossRef](#)] [[PubMed](#)]
59. ICOM. *Museum Storage Around the World*; Mairesse, F., Théobault, M., Eds.; ICOM: Paris, France, 2024. Available online: <https://icom.museum/en/news/museum-storage-around-the-world/> (accessed on 1 March 2025).
60. Thunberg, J.; Emmerson, N.; Watkinson, D. The impact of temperature on the rate of bronze disease between 10 °C and 60 °C. In *Metal 2025: Proceedings of the International Conference on Metals Conservation, Cardiff, Wales, UK, 1–5 September 2025*; Emmerson, N., Thunberg, J., Watkinson, D., Eds.; Cardiff Studies in Archaeology and Conservation: Cardiff, UK, 2025; pp. 173–180.
61. Watkinson, D.; Rimmer, M. Quantifying effectiveness of chloride desalination treatments for archaeological iron using oxygen measurement. In *Proceedings of the Metal 2013 Interim Meeting of the International Council of Museums Committee for Conservation Metal Working Group, Edinburgh, UK, 16–20 September 2013*; Hyslop, E., Gonzalez, V., Troalen, L., Wilson, L., Eds.; ICOM-CC: Edinburgh, UK, 2013; pp. 95–102.
62. Emmerson, N.J.; Seifert, J.H.; Watkinson, D.E. Refining the use of oxygen consumption as a proxy corrosion rate measure for archaeological and historic iron. *Eur. Phys. J. Plus* **2021**, *135*, 546. [[CrossRef](#)]

63. Frost, R.; Williams, P.; Klopogge, T.; Martens, W. Raman spectroscopy of the copper chloride minerals nantokite, eriochalcite and claringbullite—Implications for copper corrosion. *Neues Jahrb. Mineral. Abh.* **2003**, *10*, 433–445. [\[CrossRef\]](#)
64. Tian, H.; Wang, M.; Zhang, J.; Ma, Y.; Cui, H.; Zhao, J.; Dong, Q.; Cui, Q.; Liu, B. Pressure-Induced Variation of the Crystal Stacking Order in the Hydrogen-Bonded Quasi-Two-Dimensional Layered Material Cu(OH)Cl. *Materials* **2021**, *13*, 5019. [\[CrossRef\]](#)
65. Schlüter, J.; Klaska, K.-H.; Gebhard, G. Belloite, Cu(OH)Cl, a new mineral from Sierra Gorda, Antofagasta, Chile. *Neues Jahrb. Mineralogie. Monatshefte* **2000**, *2*, 67–73.
66. Sharkey, J.B.; Lewin, S.Z. Thermochemical Properties of the Copper (II) Hydroxychlorides. *Thermochim. Acta* **1972**, *3*, 189–201. [\[CrossRef\]](#)
67. Zheng, X.-G.; Yamauchi, I.; Kitajima, S.; Fujihala, M.; Maki, M.; Lee, S.; Hagihala, M.; Kamiyama, T.; Kawae, T. Two-dimensional triangular-lattice Cu(OH)Cl, belloite, as a magnetodielectric system. *Phys. Rev. Mater.* **2018**, *2*, 104401.
68. Cudennec, Y.; Riou, A.; Gérault, Y.; Lecerf, A. Synthesis and Crystal Structures of Cd(OH)Cl and Cu(OH)Cl and Relationship to Brucite Type. *J. Solid State Chem.* **2000**, *151*, 308–312. [\[CrossRef\]](#)
69. Liu, Y.; Ren, W.; Cui, H. Large-scale synthesis of paratacamite nanoparticles with controlled size and morphology. *Micro Nano Lett.* **2011**, *6*, 823–826. [\[CrossRef\]](#)
70. Engelbrekt, C.; Malcho, P.; Anderson, J.; Zhang, L.; Stahl, K.; Li, B.; Hu, J.; Zhang, J. Selective synthesis of clinoatacamite Cu<sub>2</sub>(OH)<sub>3</sub>Cl and tenorite CuO nanoparticles by pH control. *J. Nanoparticle Res.* **2014**, *16*, 562. [\[CrossRef\]](#)
71. Frost, R.; Martens, W.; Klopogge, T.; Williams, P. Raman spectroscopy of the basic copper chloride minerals atacamite and paratacamite—Implications for the study of copper, brass and bronze objects of archaeological significance. *J. Raman Spectrosc.* **2002**, *33*, 801–806. [\[CrossRef\]](#)
72. Martens, W.; Frost, R.L.; Williams, P.A. Raman and infrared spectroscopic study of the basic copper chloride minerals—implications for the study of the copper and brass corrosion and “bronze disease”. *Neues Jahrb. Mineral. Abh.* **2003**, *178*, 197–215. [\[CrossRef\]](#)
73. Feifer, R.A.; Schiffer, J. Vibrational Analysis of Copper Chloride Dihydrate. *J. Chem. Phys.* **1969**, *50*, 21–25. [\[CrossRef\]](#)
74. Feifer, R.A.; Schiffer, J. Intermolecular Coupling of Water Molecules in Copper Chloride Dihydrate. *J. Chem. Phys.* **1971**, *54*, 5097–5102. [\[CrossRef\]](#)
75. Medeiros, F.E.O.; Araujo, B.S.; Ayala, A.P. Raman spectroscopy investigation of the thermal stability of the multiferroic CuCl<sub>2</sub> and its hydrated form. *Vib. Spectrosc.* **2018**, *99*, 1–6. [\[CrossRef\]](#)
76. Rimmer, M.; Thickett, D.; Watkinson, D.; Ganiaris, H. Guidelines for the Storage and Display of Archaeological Metalwork. English Heritage. 2013. Available online: [https://orca.cardiff.ac.uk/id/eprint/61283/1/Storage\\_Display\\_Metalwork\\_2ndPP.pdf](https://orca.cardiff.ac.uk/id/eprint/61283/1/Storage_Display_Metalwork_2ndPP.pdf) (accessed on 24 January 2020).
77. Pimentel, D.P. Structural and Magnetic Transformations from CuCl to Cu<sub>2</sub>Cl(OH)<sub>3</sub> Induced by H<sub>2</sub>O and CuCl<sub>2</sub>. *JETP Lett.* **2024**, *120*, 50–55. [\[CrossRef\]](#)
78. Porcu, D.; Innocenti, S.; Striova, J.; Carretti, E.; Fontana, R. Mapping Bronze Disease Onset by Multispectral Reflectography. *Minerals* **2025**, *15*, 252. [\[CrossRef\]](#)
79. Hikita, H.; Ishikawa, H.; Esaka, N. Kinetics of absorption of oxygen in aqueous cuprous chloride solutions containing hydrochloric acid. *J. Chem. Eng. Jpn.* **1981**, *14*, 372–376. [\[CrossRef\]](#)
80. Eberbach, M.C.; Huinink, H.P.; Shkatulov, A.I.; Fischer, H.R.; Adan, O.C.G. The Effect of Nanoconfinement on Deliquescence of CuCl<sub>2</sub> Is Stronger than on Hydration. *Cryst. Growth Des.* **2023**, *23*, 1343–1354. [\[CrossRef\]](#)
81. Schindelholz, E.J.; Cong, H.; Jove-Colon, C.F.; Li, S.; Ohlhausen, J.A.; Moffat, H.K. Electrochemical aspects of copper atmospheric corrosion in the presence of sodium chloride. *Electrochim. Acta* **2018**, *276*, 194–206. [\[CrossRef\]](#)
82. Tsatsouli, K. ‘Bronze disease’: The Influence of Relative Humidity on Cuprous Chloride. Master’s Thesis, School of History and Archaeology, Cardiff University, Cardiff, UK, September 2004.
83. Mannard, M. Magnesium and Copper (II) Chloride: A Curious Redox Reaction. Master’s Thesis, Indiana University of Pennsylvania, Indiana, PA, USA, December 2013.
84. Iitaka, Y.; Locchi, S.; Oswald, H.R. Die Kristallstruktur von Cu(OH)Cl. *Helv. Chim. Acta* **1961**, *44*, 2095–2103. [\[CrossRef\]](#)
85. Sharkey, J.B. The Crystal Chemistry and Properties of the Copper Hydroxychlorides. Ph.D. Thesis, New York University, New York, NY, USA, 1970.
86. Nowacki, W.; Maget, K. Zur Kristallographie von Cu(OH)Cl. *Experientia* **1952**, *8*, 55. [\[CrossRef\]](#)
87. Li, R.; Shi, Y.; Shi, L.; Alsaedi, M.; Wang, P. Harvesting water from air: Using anhydrous salt with sunlight. *Environ. Sci. Technol.* **2018**, *52*, 5398–5406. [\[CrossRef\]](#)
88. Aastrup, T.; Wadsak, M.; Schreiner, M.; Leygraf, C. Experimental in situ studies of copper exposed to humidified air. *Corros. Sci.* **2000**, *42*, 957–967. [\[CrossRef\]](#)
89. Dante, J.F.; Kelly, R.G. The Evolution of the Adsorbed Solution Layer during Atmospheric Corrosion and Its Effects on the Corrosion Rate of Copper. *J. Electrochem. Soc.* **1993**, *140*, 1890–1897. [\[CrossRef\]](#)
90. Feng, Z.; Marks, C.R.; Barkatt, A. Oxidation-Rate Excursions during the Oxidation of Copper in Gaseous Environments at Moderate Temperatures. *Oxid. Met.* **2003**, *60*, 393–408. [\[CrossRef\]](#)



91. Rice, D.W.; Peterson, P.; Rigby, E.B.; Phipps, P.B.P.; Cappell, R.J.; Tremoureux, R. Atmospheric Corrosion of Copper and Silver. *J. Electrochem. Soc.* **1981**, *128*, 275–284. [\[CrossRef\]](#)
92. Serghini-Idrissi, M.; Bernard, M.C.; Harrif, F.Z.; Joiret, S.; Rahmouni, K.; Srhiri, A.; Takenouti, H.; Vivier, V.; Ziani, M. Electrochemical and spectroscopic characterizations of patinas formed on an archaeological bronze coin. *Electrochim. Acta* **2005**, *50*, 4699–4709. [\[CrossRef\]](#)
93. Orsilli, J.; Caglio, S. Combined Scanned Macro X-Ray Fluorescence and Reflectance Spectroscopy Mapping on Corroded Ancient Bronzes. *Minerals* **2024**, *14*, 192. [\[CrossRef\]](#)
94. Matthiesen, H. Oxygen monitoring in the corrosion and preservation of metallic heritage artefacts. In *Corrosion and Conservation of Cultural Heritage Metallic Artefacts*; Dillmann, P., Watkinson, D., Angelini, E., Adriens, A., Eds.; Working Party 21 on Corrosion of Archaeological and Historical Artefacts; European Federation of Corrosion Publications Number 65; Woodhead Publishing in Materials: Cambridge, UK, 2013; pp. 368–391.
95. Sherwood, D.; Reddy, M.V.; Cole, I.; Emmanuel, B. A model to estimate moisture distribution in porous oxides as a function of atmospheric conditions. *J. Electroanal. Chem.* **2014**, *725*, 1–6. [\[CrossRef\]](#)
96. King, F.; Kolar, M.; Shoesmith, D.W. Modelling the effects of porous and semi-permeable layers on corrosion processes; Paper no. 380. In Proceedings of the CORROSION 1996, Denver, CO, USA, 25–29 March 1996.
97. Garverick, L. *Corrosion in the Petrochemical Industry*, 2nd ed.; ASM International—The Materials Information Society: Materials Park, OH, USA, 1994.
98. Thunberg, J.C. Large Collections of Small Metal Objects: Managing their preservation via desiccated microclimates. In *Bridging the Gap: Corrosion Science for Heritage Contexts*; Neff, D., Grassini, S., Watkinson, D., Emmerson, N., Eds.; European Federation of Corrosion; Woodhead Publishing: London, UK, 2025.
99. Thunberg, J.; Emmerson, N.; Watkinson, D. Desiccated microclimates for heritage metals: Refining procedures for use of silica gel. *Heritage* **2025**, *8*, 240. [\[CrossRef\]](#)

**Disclaimer/Publisher’s Note:** The statements, opinions and data contained in all publications are solely those of the individual author(s) and contributor(s) and not of MDPI and/or the editor(s). MDPI and/or the editor(s) disclaim responsibility for any injury to people or property resulting from any ideas, methods, instructions or products referred to in the content.